COMPACT STUBS AND FILTERS FOR MICROMACHINED COPLANAR WAVEGUIDE

Part A

Thomas Weller and Linda Katehi

August 1995

Compact Stubs and Filters for Micromachined Coplanar Waveguide

Thomas M. Weller   Linda P. B. Katehi

The Radiation Laboratory, University of Michigan
1301 Beal Avenue, Ann Arbor, MI 48109-2122 U.S.A.
Contract Number PF-399 - Final Report (August 1995)

Abstract - This report presents new CPW-type stub and filter configurations which are useful for compact microwave circuit design. It is shown that conventional open- and short-end quarter wavelength stubs can be shortened by a factor of three by folding the center conductor. Also, narrow-band open-end stubs and filters are demonstrated which have thin-film overlay capacitors integrated across the stub sections. In this work the circuits have been implemented using microshield transmission line, a geometry in which a 1.4 μm-thick dielectric membrane supports coplanar conducting lines virtually in free-space. The new stub configurations are also suitable for standard substrate-supported CPW.

I. INTRODUCTION

Micromachining techniques have recently been utilized for transmission line design, resulting in high performance components which operate from microwave to sub-mm wave frequencies [1, 2]. One such line, microshield, is a partially shielded geometry which is micromachined in a silicon (or GaAs) substrate and uses a 1.4 μm-thick dielectric membrane to support coplanar conducting lines essentially in free-space (Figure 1). Another micromachined geometry is the substrate-supported coplanar waveguide with integrated shielding cavities; a version with only a lower cavity is also shown in Figure 1. As demonstrated by Drayton and Katehi [3] the self-enclosed nature of this line results in minimal parasitic radiation and can eliminate problems related to package resonances.

Although high performance is generally a prime system requirement, many of today's RF applications, such as wireless communications, also demand architectures with high density layouts. Two of the main obstacles in achieving this goal are circuit crosstalk and component size. In the case of CPW (coplanar waveguide) based tuning stub elements, crosstalk can be minimized by using series stubs which are patterned in the center conductor, as opposed to shunt stub configurations. These types of stubs are useful for switches [4], filters [5, 6], and DC and LO blocks. At low frequencies or on low permittivity substrates, however, they tend to occupy considerable amounts of space since they are often designed to be a quarter-wavelength long. As a solution to this problem, the concept of *folded* series stubs is introduced herein. It will be demonstrated that these miniature configurations provide a narrower bandwidth than the conventional geometries and are only one third as long. This size reduction is particularly important for implementations
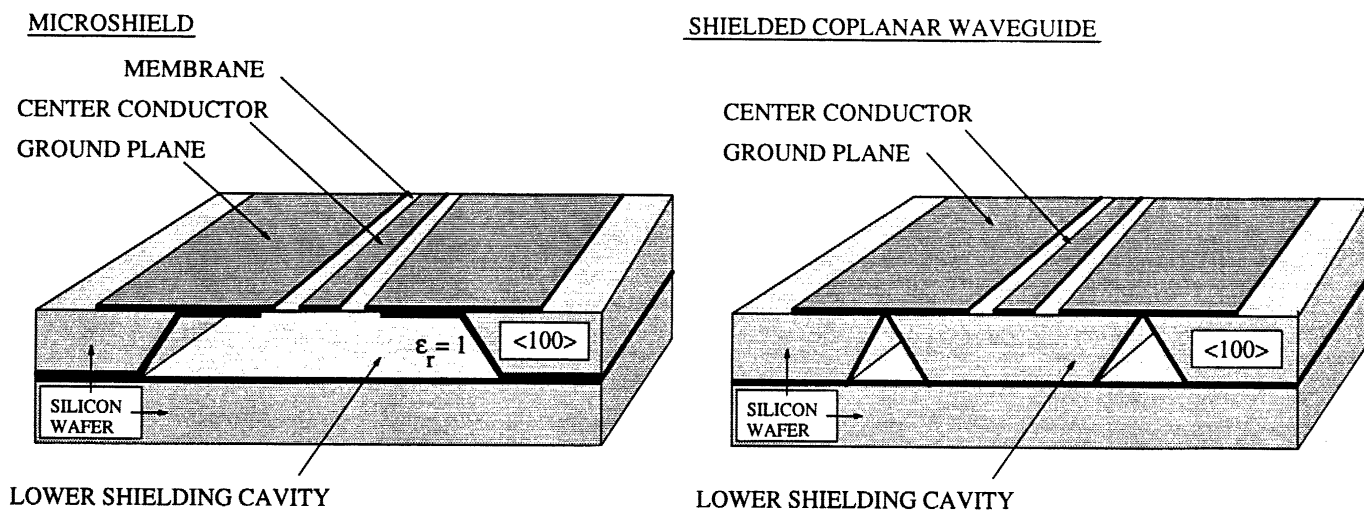
1

Figure 1: Micromachined transmission lines: microshield and shielded coplanar waveguide.

using the membrane-supported microshield line, since the relative permittivity of microshield is very close to 1. For completeness, it will be demonstrated that the folding technique can be utilized with the substrate-supported, shielded coplanar waveguide, as well. Also presented in this report is a new technique for designing narrow-band stubs, in which distributed element stubs are combined with lumped element, MIM (metal-insulator-metal) capacitors. Measured 3-dB bandwidths of around 16% have been obtained using circuits which are $\lambda/4$ in length, demonstrating a significant reduction over the 100% bandwidth of a comparable series open-end stub.

It is noted that the contents of this report represent an accumulation of material which is taken from references [7, 8, 9].

II. COMPACT STUB DESIGNS

II.1 Short-End Stubs

A conventional short-end series stub in CPW can be realized by deforming the center conductor with two shorted slots which are connected to the center conductor-to-ground plane slots (Figure 2). At the resonant frequency, these inner slots are a quarter wavelength long and thus the short circuit at point A is transferred to an open-circuit at point B, resulting in a band-stop response. Using the folded approach, the inner slots are simply folded back upon themselves one or two times. The five short-end, folded stub geometries which were studied are illustrated along with the conventional design in Figure 3. For the single-folded approach there are two ways of interleaving the fingers, whereas there are three possible arrangements for the double-folded approach. Each pattern yields a unique frequency response, as demonstrated by the examples provided in Table 1 and the associated plots in Figures 4-9. This data contains calculated results which were generated using a full-wave moment method analysis along with experimental results for design S-D. By comparing these plots to the performance of the conventional design (S-A) shown in Figure 10, it is seen that similar behavior is obtained using Design S-D, although it is 2.4 times shorter than S-A at the first band-stop resonance. Also, the 3-dB bandwidth is reduced from 70% to 40% by using the folded design.
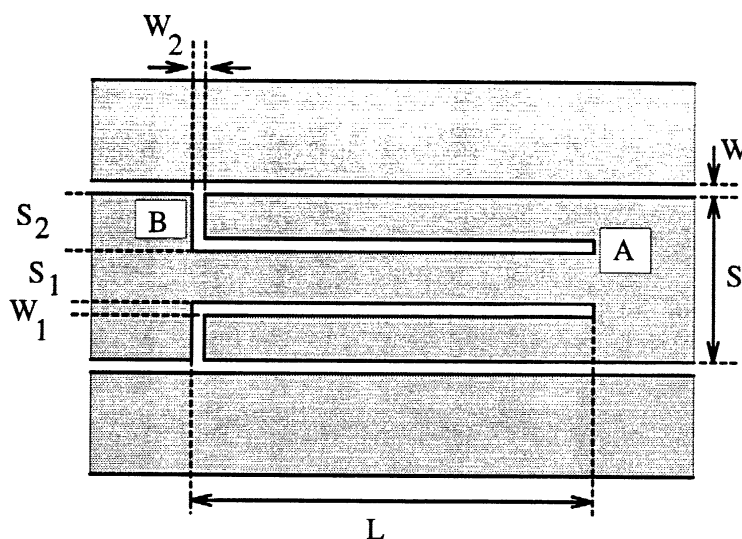
Figure 2: A microshield short-end series stub.

Design	S	W	S_1	S_2	W_1	W_2	L	ϵ_r	λ_r/L
S-A	260	20	70	75	20	20	2720	1.4	4.2
S-B	260	20	36	36	20	20	1320	1.4	7.3
S-C	260	20	36	36	20	20	1320	1.4	7.4
S-D	260	20	20	20	20	20	1020	1.4	9.9
S-E	260	20	20	20	20	20	1020	1.4	8.9
S-F1	260	20	20	20	20	20	1020	1.4	9.2
S-F2	130	80	10	10	10	10	720	13.1	9.8

Table 1: Parameters for conventional (S-A) and folded short-end stub designs (refer to Figure 3), where λ_r is the guide wavelength at the first band-stop resonance. The dielectric constant of 1.4 was used to simulate the microshield line for the dimensions given in the table. All dimensions are in μm.

The other four configurations have somewhat different characteristics and provide varying degrees of miniaturization.

In order to show that the folding technique is also applicable to standard substrate-supported CPW, a design on GaAs is included in Table 1 (S-F2). A potential problem with the high permittivity substrate is parasitic radiation, since a relatively wide center conductor is required to accommodate the multi-finger geometry. The performance can be greatly improved, however, by utilizing the micromachining techniques reported by Drayton et al. [3] to integrate a lower shielding cavity. This type of cavity has been assumed in the analysis of design S-F2, the results of which are shown in Figure 9. The cavity size in this case was 800 μm wide by 500 μm deep (see Figure 1), which was small enough such that a shorter version of the same geometry could be made to operate very well up to at least 35 GHz. At lower frequencies (e.g. below 15 GHz), larger line widths can be used without significant radiation effects, making the shielding cavities unnecessary.
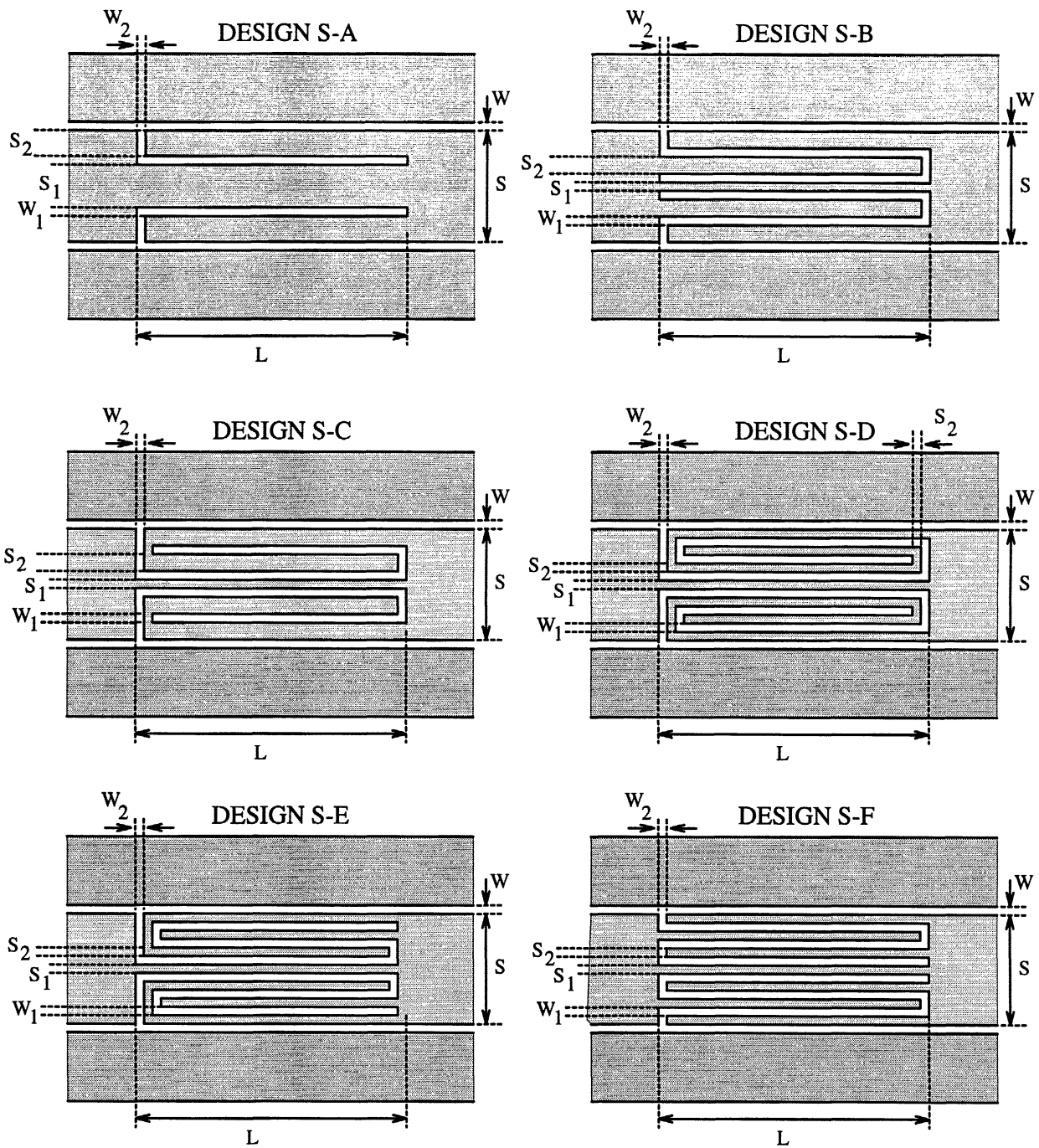
Figure 3: Conventional and compact short-end series stub configurations. S_1 refers to the center finger width and S_2 refers to the width of all outer fingers.
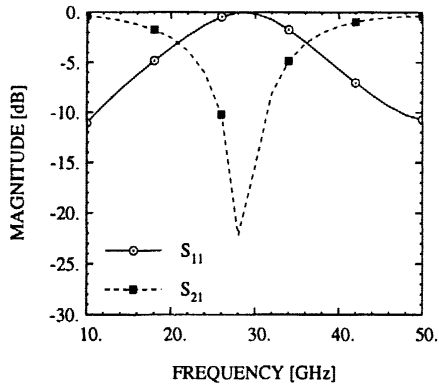
4

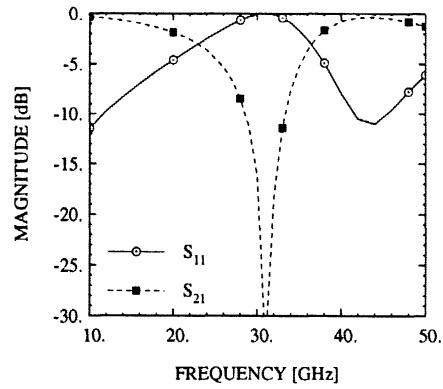Figure 4: Performance of stub S-B.
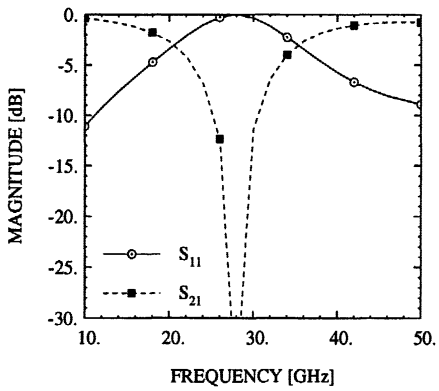

Figure 7: Performance of stub S-E.

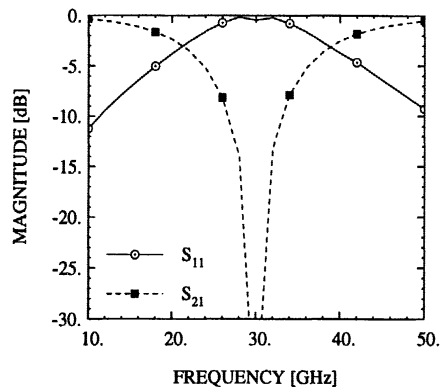Figure 5: Performance of stub S-C.

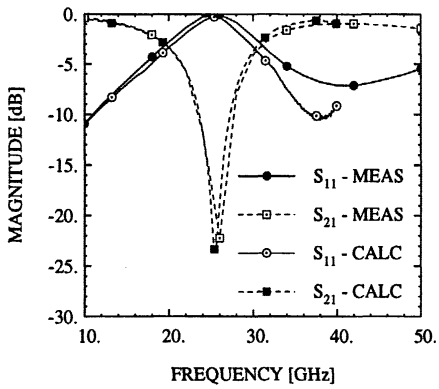Figure 8: Performance of stub S-F1.
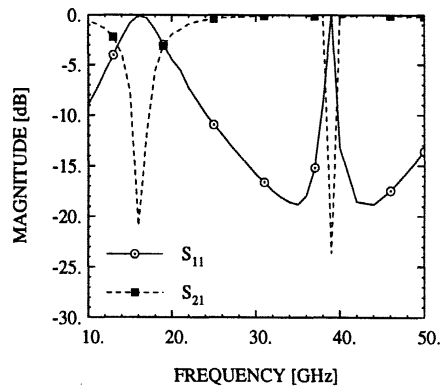

Figure 6: Performance of stub S-D.

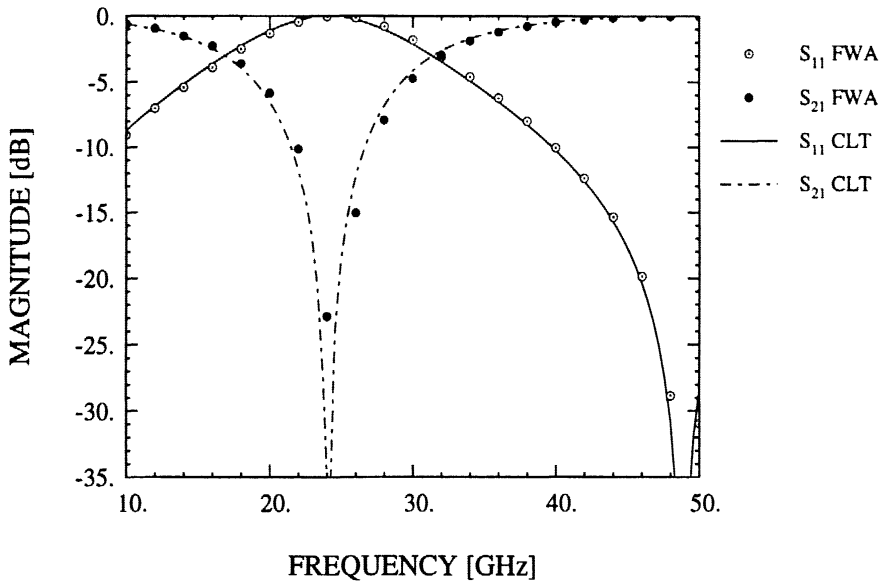

Figure 9: Performance of stub S-F2.

Figure 10: Comparison between the results from a full-wave moment method analysis (FWA) and a coupled line technique based on quasi-static approximations (CLT) [9]. The circuit is a microshield short-end series stub (design S-A from Table 1).

II.2 Open-End Stubs

The open-end series stub is identical to the short-end stub except that the center conductor slots on either side are connected to each other. This creates an open-circuit at the ends of the slots, which transfers to a short circuit at the input port at the resonant frequency and gives a bandpass response. Along with the work on the short-end stubs, an investigation has been made into different possibilities for folded open-end stubs. In this case there is only one way of interleaving the fingers in a single-folded approach, and two ways for the double-folded geometry. These three configurations are illustrated along with the conventional design in Figure 11.

As shown by the examples provided in Table 2 and the corresponding plots in Figures 12-18, each pattern exhibits a different frequency response. It can be seen from the last column of the table that the performance of the conventional design (O-A) is achieved using a stub with a total length of around $\lambda_r/10$ (O-D1 through O-D3). It is also observed that the implementations which are essentially interdigitated capacitors (O-B1, O-B2, O-C) have characteristics that are distinctly different than the conventional stub. Finally, as with the short-end stubs, a lower shielding cavity of dimensions 800 μm by 500 μm has been included in the designs on the high permittivity substrate.

The last row in Table 2 represents a circuit designed to resonate at approximately 330 GHz. The results, shown in Figure 17, do not include the effects of a lower shielding cavity and yet the radiation loss is still low enough that the performance is maintained through the first resonance. Using the approximation that the total ground plane separation should be less than $\lambda/10$, this design has an upper frequency for quasi-TEM operation of around 300 GHz. Assuming the minimum line width to be 5 μm, this represents the practical limit for the microshield, double-folded stub geometry.

Design	S	W	S_1	S_2	W_1	W_2	L	ϵ_r	λ_r/L
O-A	260	20	70	75	20	20	2720	1.4	4.2
O-B1	260	20	36	36	20	20	2320	1.4	5.2
O-B2	90	60	10	10	10	10	900	13.1	4.9
O-C	260	20	20	20	20	20	1140	1.4	6.0
O-D1	260	20	20	20	20	20	1140	1.4	10.0
O-D2	130	80	10	10	10	10	550	13.1	10.0
O-D3	65	20	5	5	5	5	86	1.4	9.6

Table 2: Parameters for conventional (O-A) and folded open-end stub designs (refer to Figure 11), where λ_r is the guide wavelength at the first band-pass resonance. All dimensions are in μm.
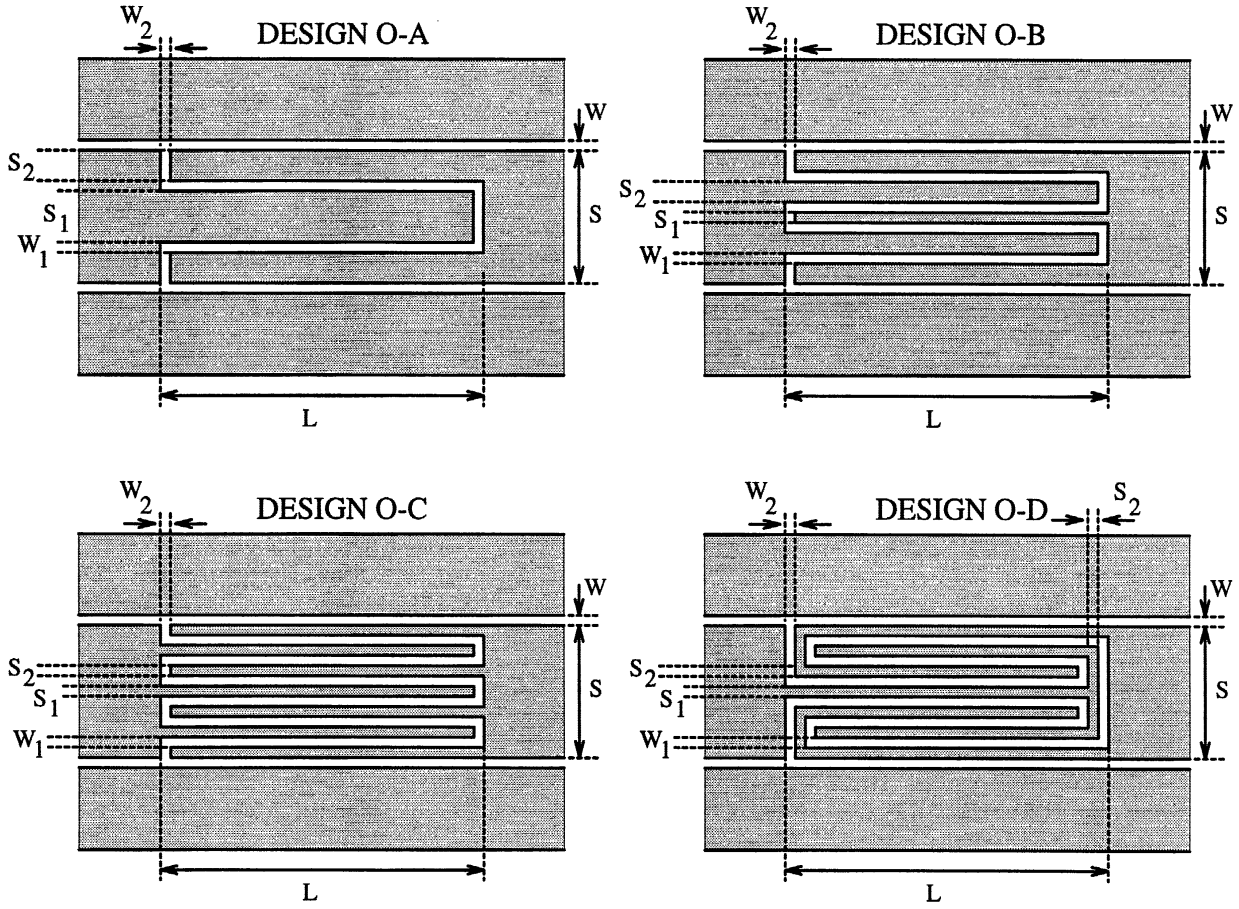

Figure 11: Conventional and compact open-end series stub configurations. S_1 refers to the center finger width and S_2 refers to the width of all outer fingers.
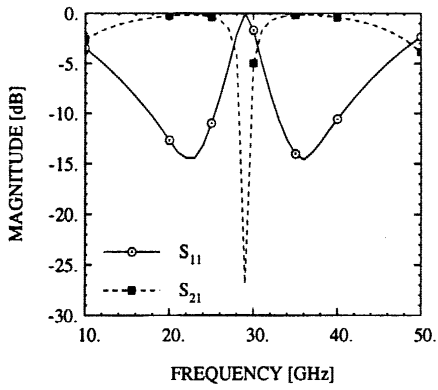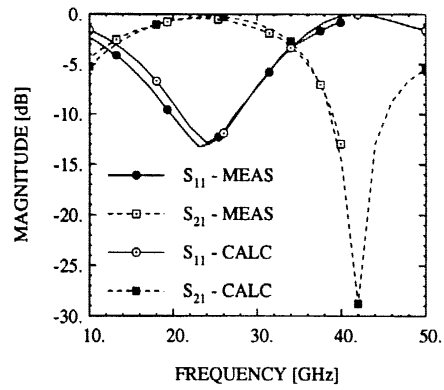
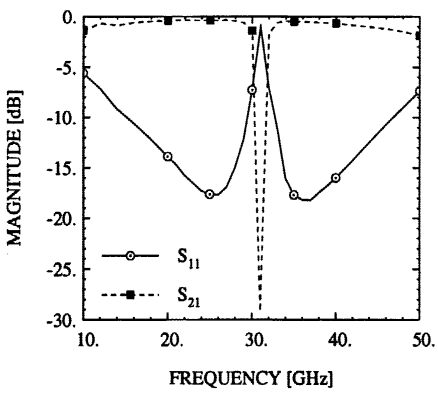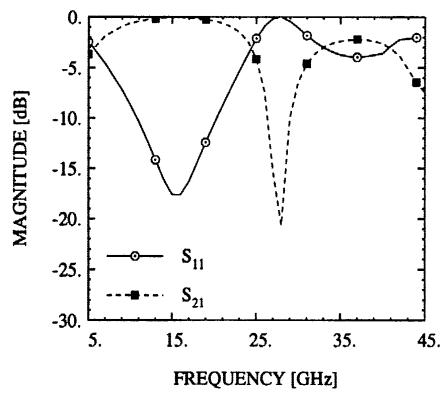Figure 12: Performance of stub O-B1.

Figure 13: Performance of stub O-B2.

Figure 14: Performance of stub O-C.
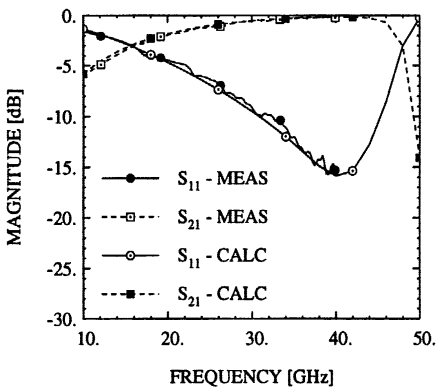

Figure 15: Performance of stub O-D1.

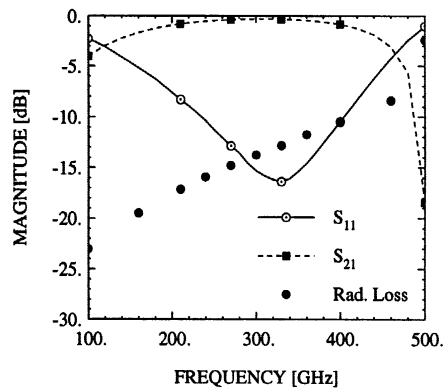Figure 16: Performance of stub O-D2.

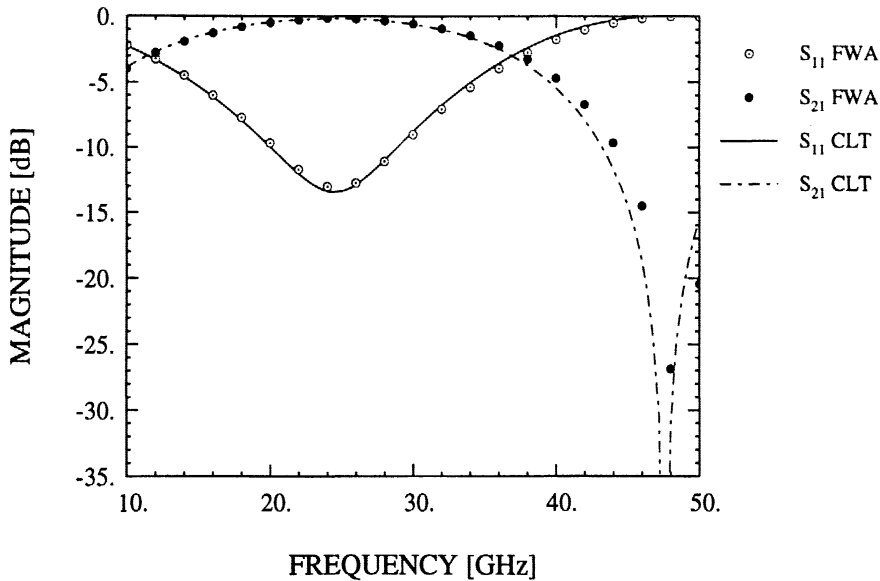
Figure 17: Performance of stub O-D3.

Figure 18: Comparison between the results from a full-wave moment method analysis (FWA) and a coupled line technique based on quasi-static approximations (CLT) [9]. The circuit is a microshield open-end series stub (design O-A from Table 2).

II.3 Hybrid Stubs

In addition to the folded stub configurations, an alternative design approach has been developed which emphasizes bandwidth reduction along with circuit miniaturization. The target applications are those in which the quarter-wavelength resonance of the series stubs are utilized for frequency separation, as in the use of the open-end stub as a band-pass filter. With conventional or folded series open-end stubs, the 3-dB bandwidth typically ranges between 70% to over 100%, depending on the substrate and the stub geometry. This may force the circuit designer to cascade multiple stubs in series in order to achieve a smaller passband, leading to circuit dimensions around 0.5 λ_g or greater. An inherent property of the open-end stub, however, is that the bandwidth can be decreased by increasing the shunt capacitance. This fact motivated the implementation of the "hybrid" stub geometry, in which lumped element capacitors are integrated with the distributed element stub.

The basic configuration consists of two cascaded stubs, with the second stub reversed relative to the first (Figure 19). Along the length of the stubs, MIM (metal-insulator-metal) overlay capacitors are deposited in shunt with the outer stub arms and the upper ground planes. This is believed to be a unique approach for combining lumped and distributed elements for filter applications, although variations of the technique have been presented by previous authors (e.g. [10, 11]). In this research, the capacitor dielectric was a silicon monoxide (SiO) layer which was approximately 1 μm thick.

Several different designs are detailed in Table 3, and the predicted and measured performance of the stubs is presented in Figures 20-25. For the purpose of comparison, the performance of a design which has no capacitors (H-O1) is shown in Figure 20. The center frequency is 60 GHz, corresponding to the quarter-wavelength frequency of each of the open-end stubs. In design H-O2, 17.5 pF capacitors have been integrated 410 μm from the ends of each stub, resulting in a pass-band resonance at 37 GHz and a 3-dB bandwidth of 26% (Figure 21). By moving the capacitors closer
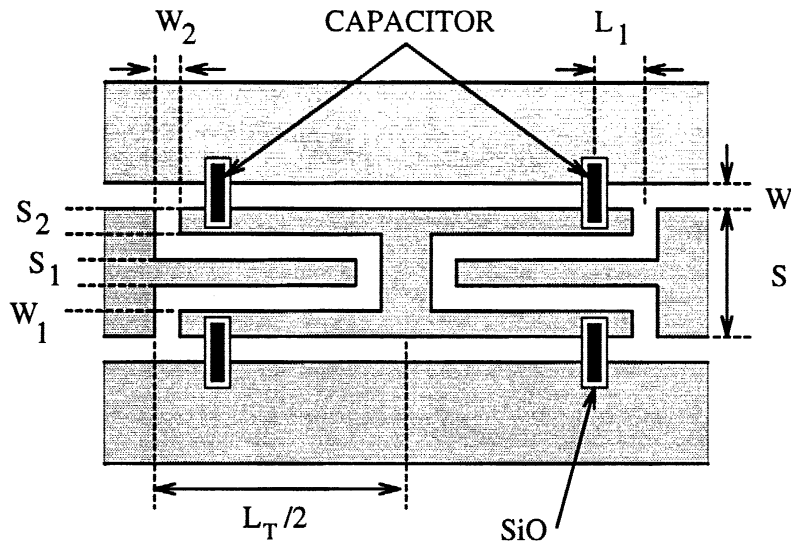
9

W₂ CAPACITOR L₁

S₂
S₁
W₁

W

S

L_T/2

SiO

Figure 19: Hybrid open-end stub configuration.

to the ends of the stubs, the passband is shifted down to 32 GHz, as demonstrated by design H-O3 (Figure 22). This trend indicates that the lowest resonant frequency, for a given stub length and capacitor size, is obtained by positioning the capacitors at the stub ends. An explanation for this can be found by breaking down the circuit into simple resonators, each one formed by a series capacitance (the stub section) combined with a shunt capacitance (the overlay capacitors). Placing the capacitors at the end of each stub maximizes the distance between resonators, thus reducing the resonant frequency. By examining the curves in Figure 23, it is observed that the resonant frequency can also be decreased by utilizing larger capacitors. This is accompanied by a significant reduction in the bandwidth, however, and the insertion loss naturally tends to increase.

A method to lower the resonant frequency and keep the insertion loss down is to use stubs with a higher characteristic impedance, as in designs H-O5 and H-O6. These stubs have broader 3-dB bandwidths than stubs with lower characteristic impedance, since the shunt capacitance is smaller. Thus, the same size overlay capacitor yields a wider bandwidth and lower insertion loss; this is seen by comparing the characteristics of designs H-O3 and H-O5. The last design in the table (H-O6) shows that a resonant frequency at 25.5 GHz can be achieved with 1 dB insertion loss and 30 dB rejection at 5 GHz. An open-end series stub of approximately the same length exhibits 0.25 dB loss at 27 GHz and only 7-9 dB rejection at 5 GHz.

Design	S	W	S_1	S_2	W_1	W_2	L_1	C, fF	ϵ_r	λ_r/L_T	$S_{21,max}$	%BW
H-O1	260	20	40	85	25	100	-	0.0	1.4	2.28	-	76
H-O2	260	20	40	85	25	100	410	17.5	1.4	2.98	-0.83	26
H-O3	260	20	40	85	25	100	170	17.5	1.4	3.15	-0.90	24
H-O4	260	20	40	85	25	100	170	35.0	1.4	3.83	-1.80	10.5
H-O5	260	70	40	85	25	100	170	17.5	1.1	3.70	-0.50	28
H-O6	260	70	40	85	25	100	170	25.8	1.1	4.45	-1.00	18

Table 3: Parameters for hybrid open-end stub configurations, all of which have a total length of L_T=2500 (refer to Figure 19). The passband insertion loss, $S_{21,max}$ (dB), is included for designs which have been characterized experimentally. All dimensions are in μm.
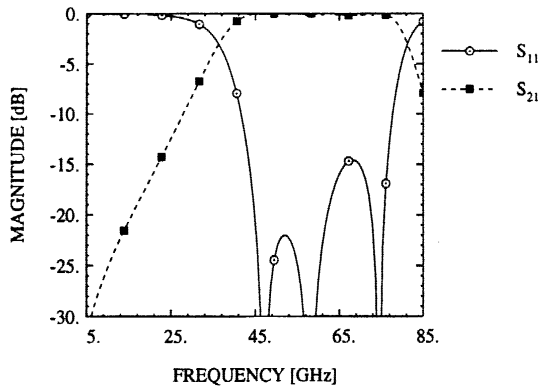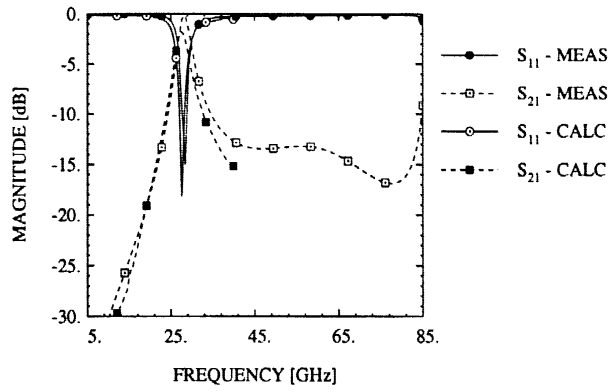
Figure 20: Performance of stub H-O1.

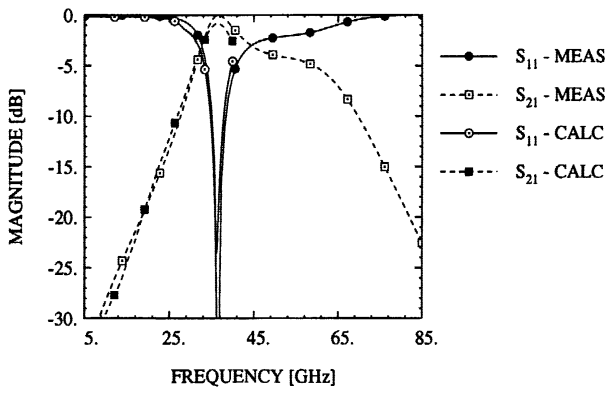Figure 23: Performance of stub H-O4.

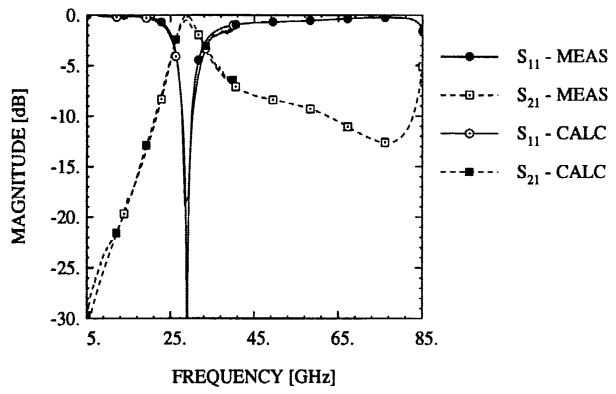Figure 21: Performance of stub H-O2.
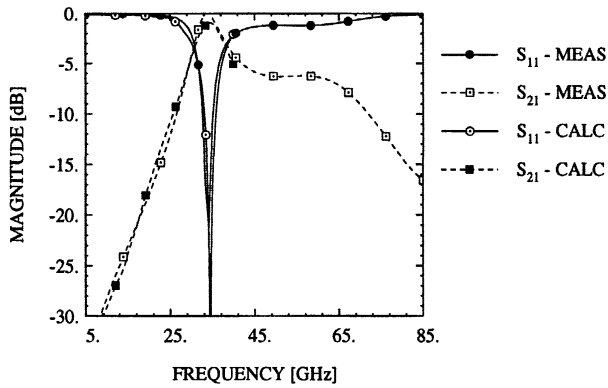

Figure 24: Performance of stub H-O5.

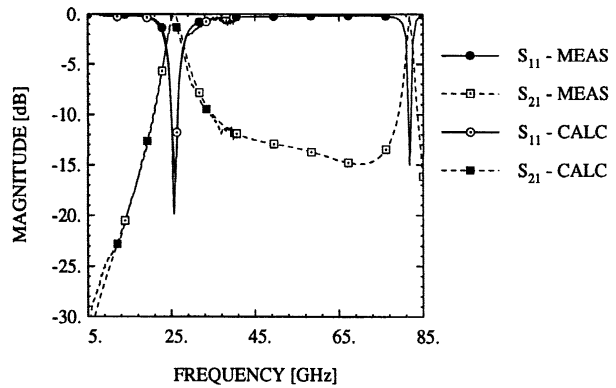Figure 22: Performance of stub H-O3.

Figure 25: Performance of stub H-O6.

12

III. BAND-PASS FILTER DESIGNS

A variety of methodologies exists for the implementation of planar bandpass filters. In microstrip or stripline form it is common to utilize a configuration of edge-coupled strips, as with the filters presented by Chi and Robertson [12, 13]. For coplanar waveguide applications, filters using a combination of series and shunt tuning stubs, such as the conventional geometries presented in the preceding sections, have received considerable attention (e.g. [14, 15, 16]). In a slightly different manner, electrically-short series open-end stubs have been utilized as admittance inverters between $\lambda_g/2$ resonators in end-coupled designs [6]. The main objectives of this research, however, were to develop filters with minimal lateral width to keep the cavity dimensions small, and to achieve reasonably short longitudinal dimensions. Designs ranging in length between 0.5-0.8 λ_g, and with bandwidths between 15 and 60%, will be presented herein. In all cases the measured pass-band attenuation, which includes radiation and conductor loss, has an uncertainty of less than $\pm$ 0.1 dB.

The different band-pass filter implementations are illustrated in Figure 26 and some of the performance characteristics are listed in Table 4. The first design consists of three open-end stubs which are cascaded in series, with each stub being approximately $\lambda_g/4$ in length at the center frequency [9]. The measured response (Figure 27) shows an insertion loss of only 1.0 dB from 22-32 GHz, which is competitive with the best waveguide bandpass filters using suspended stripline [17]. The attenuation of this filter could be reduced by using thicker metalization[1] or larger slot widths to minimize the conductor loss. In order to predict the performance, the scattering parameters of a single stub were determined using a full-wave analysis, and the filter was treated as three non-coupled elements. The agreement between the measured and calculated results is nearly exact at the high end of the band, and the shift of approximately 1 GHz at the low end of the band is consistent with the comparison for a single stub [9]. The good agreement indicates that there is very little electromagnetic coupling between the stubs, even though the separation between them is only 150 μm.

The next two designs in Table 4 are based on the folded open-end stub geometry, and their performance is illustrated in Figures 28 and 29. It is immediately apparent that these 5-section filters provide greater out-of-band rejection than the previous 3-section design, and yet they are only 65% as long due to the use of the compact stub. Design 2 has a measured 3-dB bandwidth of 32% and a pass-band loss of 2 dB, while design 3 has a bandwidth of 40% and only 1 dB insertion loss. The single difference between the filters is the outer slot width, which is 20 μm and 70 μm for designs 2 and 3, respectively. This slot-width effect is characteristic of all the series stub-based designs, and while some decrease in loss is expected as the bandwidth increases, a substantial part of the improvement is due to the lower conductor loss of the higher impedance line. In comparing the measured and predicted results, it is seen that the center frequencies are within 0.5-1 GHz, but that a discrepancy of 5% in the bandwidth exists in both cases. This is believed to result from modeling the filters as non-coupled resonators, as explained for the previous case. A complete model of the entire filter would certainly be a more accurate comparison, however the size of the system becomes impractical to solve using the formulation employed in this work.

The last two designs in Table 4 consist of a series combination of the hybrid open-end stub configuration. In comparison to the previous geometries, this type of filter is more appropriate for achieving narrow bandwidths and fast roll-off in the rejection at the low end of the band. These

---

[1]All circuits fabricated in this study had a metalization thickness of 1 μm.

TYPE O-A
(DESIGN 1)

2500   150

L$_T$

TYPE O-D
(DESIGNS 2,3)

1140   40   300

L$_T$

TYPE H-O
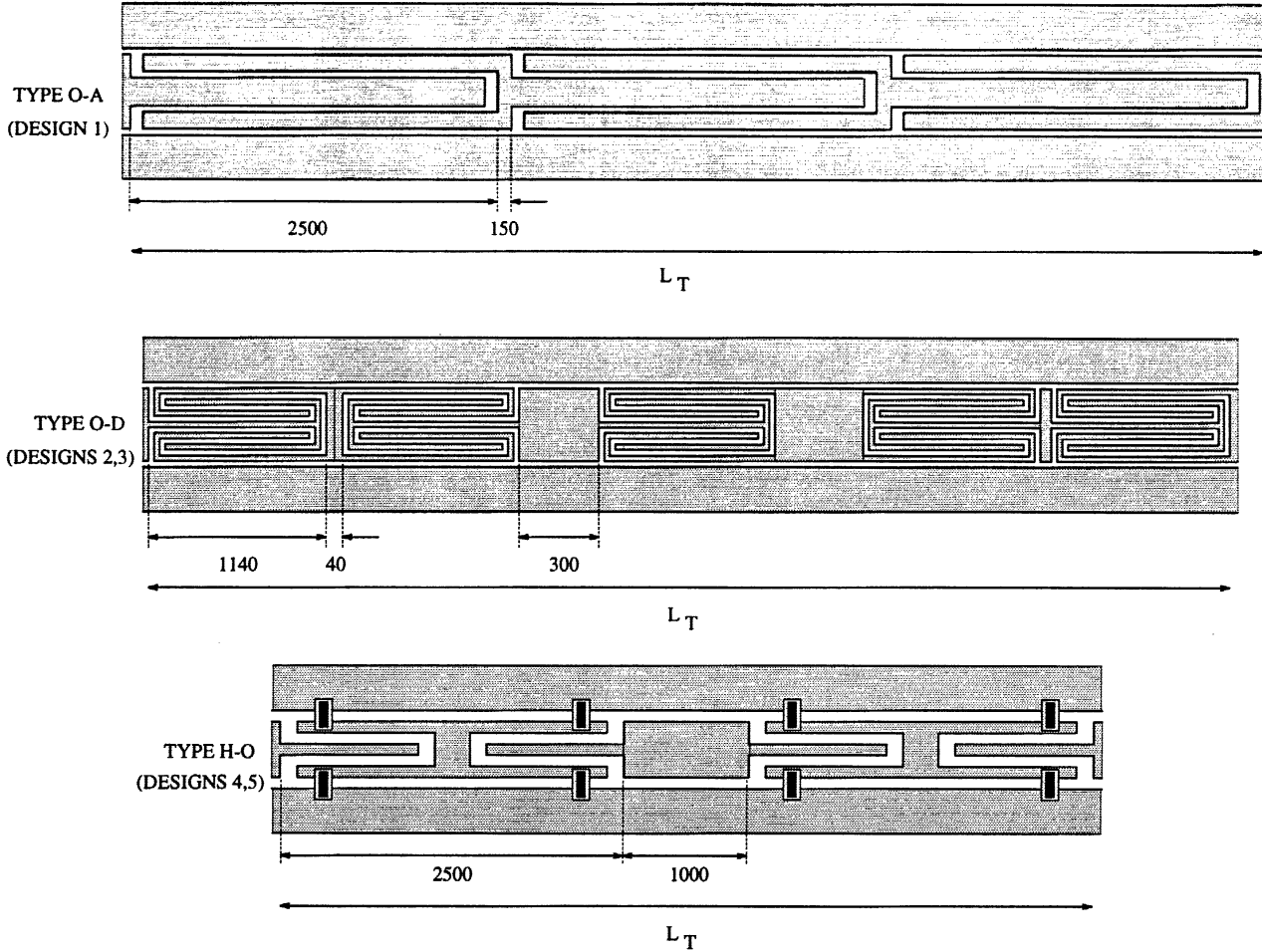(DESIGNS 4,5)

2500   1000

L$_T$

Figure 26: Band-pass filter configurations studied in this research. Element lengths and separations are specified in microns.

advantages come at the expense of the high-end rejection, as seen in Figures 30 and 31. Design 4 has a bandwidth of 17% and a pass-band loss of 0.9 dB. Upon re-examining the design, it was found that the 1000 μm separation between the elements (see Figure 26) caused the second pass-band to shift down in frequency and degraded the out-of-band response. In design 5 the separation was reduced to 40 μm, resulting in improved high-end rejection and similar low-end and pass-band performance. The predicted response from a coupled line analysis of this filter [9] is shown in Figure 31. Compared to design 1, the filter exhibits 23 dB more rejection at 0.5f$_o$ and 4 dB more rejection at 1.5f$_o$, although the overall length is 60% shorter.

IV. CONCLUSION

Microwave applications such as wireless communications depend on high performance components and high density architectures. To help meet this requirement, this report has presented compact series stub configurations for CPW which are up to 2.5 times smaller than conventional implementations. Designs which use the membrane-supported microshield line have been validated at Ka-band through comparisons of experimental data and results from a full-wave analysis. Using the same theoretical model, it has been determined that the upper frequency limit for the microshield stub is approximately 330 GHz. Another new approach was developed that combines integrated

14

Design	Type	f_o	L_T at f_o, λ_g	%BW	$S_{21,max}$	S_{21} @ $0.5f_o$	S_{21} @ $1.5f_o$
1	O-A	29	0.80	58/55	-1.0	-17	-17
2	O-D	24	0.51	32/27	-2.0	-29	-32
3	O-D	25	0.53	44/38	-1.0	-20	-21
4	H-O	28	0.56	17/15	-0.9	-36	-18
5	H-O	29	0.47	17	-	-40	-21

Table 4: Parameters for microshield band-pass filter designs (refer to Figure 26). The passband insertion loss, $S_{21,max}$ (dB), is included for designs which have been characterized experimentally. In the %BW column, the first number is the measured 3-dB bandwidth and the second is the predicted value.
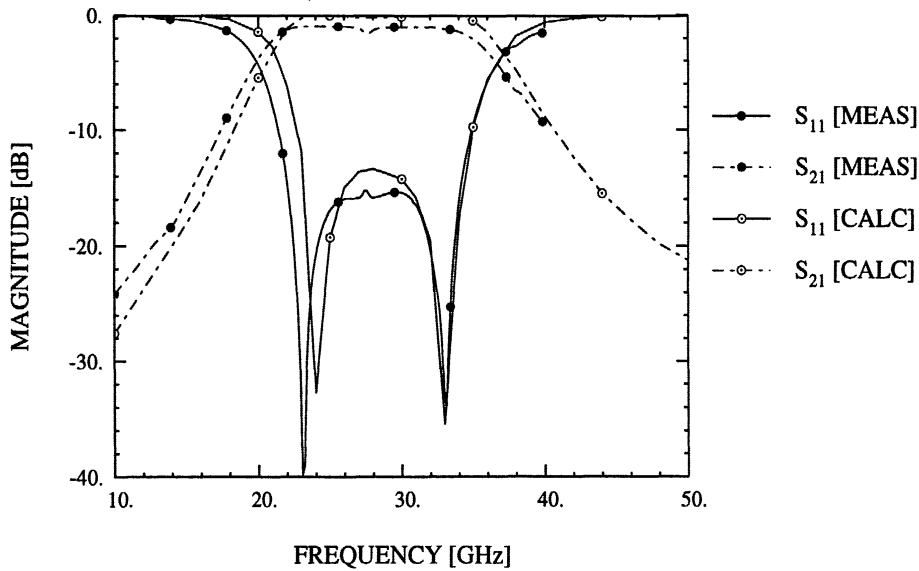

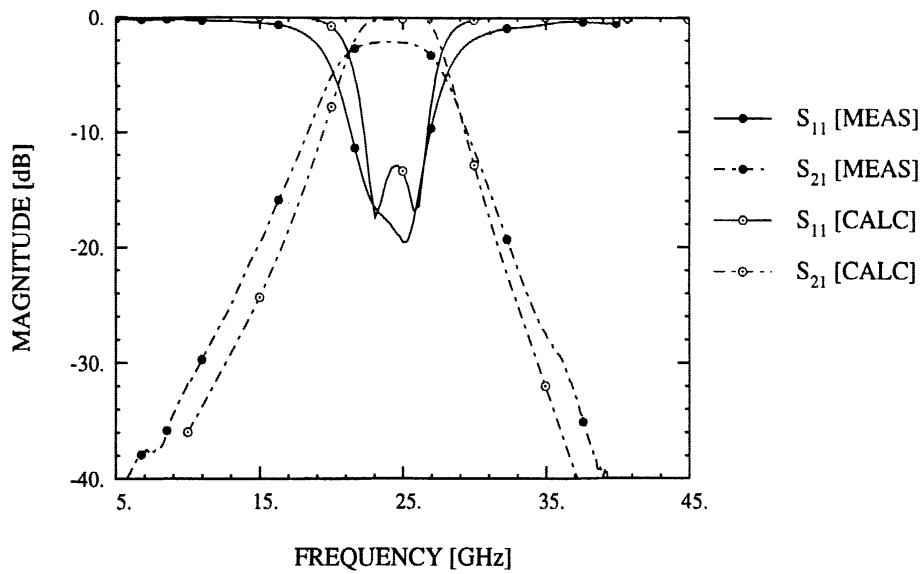Figure 27: S-parameters for bandpass filter design 1 in Table 4.

15

Figure 28: S-parameters for bandpass filter design 2 in Table 4. The folded open-end stub dimensions are the same as those of design O-D1 in Table 2.
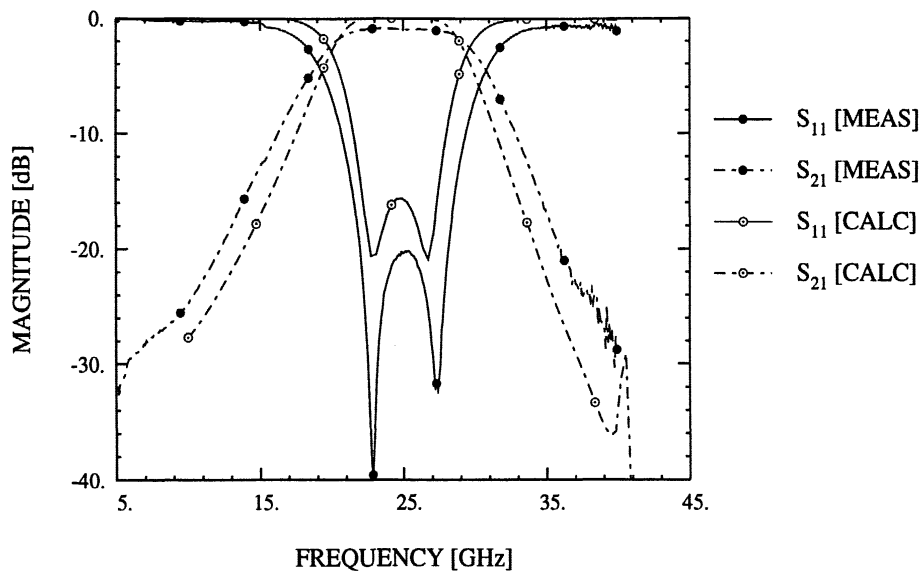

Figure 29: S-parameters for bandpass filter design 3 in Table 4. The folded open-end stub dimensions are the same as those of design O-D1 in Table 2, except that W=70 μm.
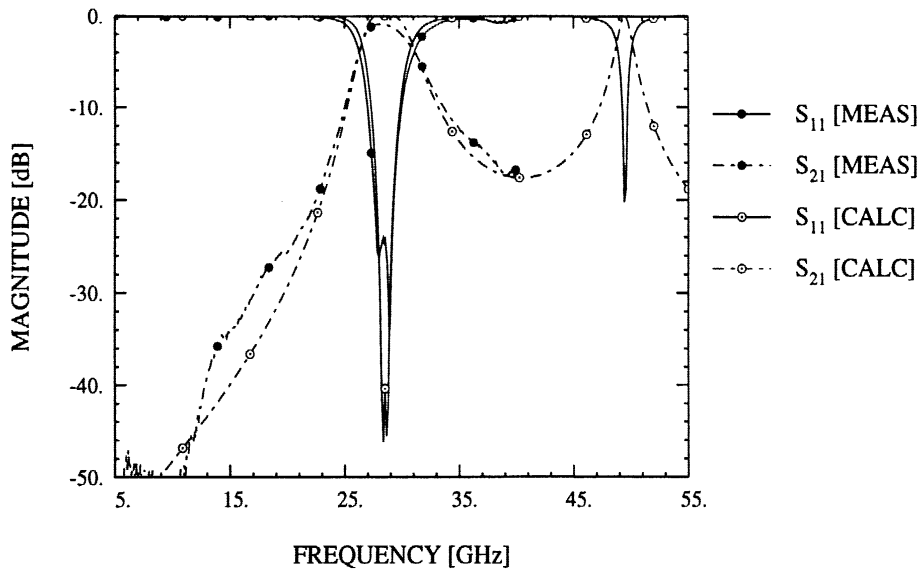
16

Figure 30: S-parameters for bandpass filter design 4 in Table 4. The hybrid stub design is the same as design H-O5 in Table 3.
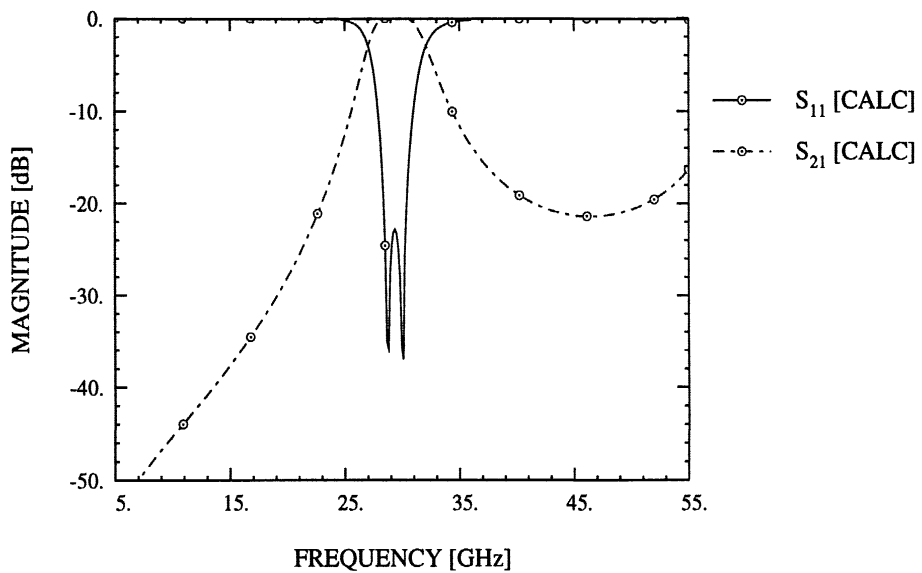

Figure 31: S-parameters for bandpass filter design 5 in Table 4, which is identical to design 4 except that all elements are separated by 40 μm.

17

thin-film capacitors with standard distributed-element stubs. For a circuit length of $\lambda/4$, these designs provide at least 20 dB more low frequency rejection than a simple tuning stub. A number of band-pass filter implementations were also pursued which employed the different types of series stubs as end-to-end resonators. These designs achieve minimum lateral width (typically around 300 μm) and lengths ranging between 0.5-0.8 λ, with bandwidths between 15-60%.

ACKNOWLEDGMENT

REFERENCES

[1] C-Y Chi and G. M. Rebeiz, "Planar Millimeter-wave Microstrip Lumped Elements Using Micromachining Techniques," 1994, *IEEE MTT-S Digest*, vol. 2, pp. 657-660.

[2] T. M. Weller, L. P. B. Katehi and G. M. Rebeiz, "A 250 GHz Microshield Bandpass Filter," 1995 *IEEE Microwave and Guided Wave Letters,* vol. 5, no. 5, pp. 153-155.

[3] R. F. Drayton and L. P. B. Katehi, "Development of Miniature Microwave Circuit Components Using Micromachining Techniques, " 1994, *IEEE MTT-S Digest*, vol. 1, pp. 225-228.

[4] P. A. R. Holder, "X-band microwave integrated circuits using slotline and coplanar waveguide," 1978, *The Radio and Electronic Engineer*, vol. 48, no. 1/2, pp. 38-42.

[5] N. Dib, P. Katehi, G. Ponchak and R. Simons, "Theoretical and Experimental Characterization of Coplanar Waveguide Discontinuities for Filter Applications," *IEEE Trans. MTT*, pp. 873-882, May 1991.

[6] D. F. Williams and S. E. Schwarz, "Design and Performance of Coplanar Waveguide Band-Pass Filters," 1983, *IEEE Trans. MTT*, vol. MTT-31, no. 7, pp. 558-566.

[7] T. M. Weller and L. P. B. Katehi, "Compact Stubs for Micromachined Coplanar Waveguide," *Proceedings of the 25th European Microwave Conference*, September 1995.

[8] T. M. Weller and L. P. B. Katehi, "Miniature Stub and Filter Designs Using the Microshield Transmission Line, " *IEEE MTT-S Digest*, 1995, Orlando, vol. 2, pp. 675-678.

[9] T. M. Weller, "Micromachined High Frequency Transmission Lines on Thin Dielectric Membranes, " Ph.D. Thesis, Radiation Laboratory, University of Michigan, 1995.

[10] T. Ishizaki, M. Fujita, H. Kagata, T. Owano and H. Miyake, "A Very Small Dielectric Planar Filter for Portable Telephones," *IEEE Trans. MTT*, vol. MTT-42, pp. 2017-2022, November 1994.

[11] R. Pregla, "Microwave Filters of Coupled Lines and Lumped Capacitances," *IEEE Trans. MTT*, vol. MTT-18, pp. 278-280, May 1970.

[12] C. Y. Chi and G. M. Rebeiz, "Planar Microwave Millimeter-Wave Lumped Elements and Coupled-Line Filters Using Micro-machining Techniques," *IEEE Trans. MTT*, vol. 43, no. 4, pp. 730-738, April 1995.

[13] S. V. Robertson, L. P. Katehi, and G. M. Rebeiz, "Micromachined Self-Packaged W-Band Bandpass Filters, " *1995 IEEE MTT-S International Microwave Symposium Digest.*

[14] K. Hettak, J.Ph. Coupez, E. Rius and S. Toutain, "A New Uniplanar Bandpass Filter Using $\lambda_g/2$ Slotline and $\lambda_g/4$ Coplanar Waveguide Resonators, " *Proceedings of the 1994 EuMC,* Cannes, vol. 2, pp. 1360-1366.

[15] K. Hettak, T. Le Gouguec, J. Ph. Coupez, S. Toutain, S. Meyer and E. Penard, "Very Compact Low Pass and Bandpass Filters using Uniplanar Structures, " *Proceedings of the 1993 EuMC,* Madrid, vol. 1, pp. 238-239.

[16] Y. Noguchi, S. Kitazawa, T. Wada, T. Ohmiyama and N. Okamoto, "A New Compact $\lambda_g/4$ Coplanar Waveguide Resonator Bandpass Filter, " *Proceedings of the 1993 EuMC,* Madrid, vol. 1, pp. 631-633.

[17] W. Menzel, "Broadband Filter Circuits Using an Extended Suspended Substrate Transmission Line Configuration," *Proceedings of the 22nd EuMC,* Helsinki, vol. 1, 1992, pp. 459-463.

PDF REPORT ON MEMBRANES

Part B

Marty Herman, Abhijit Biswas, Elzbieta Kolawa, and Beveral Tai
Jet Propulsion Laboratory

August 1995

PDF Report on Membranes

Jet Propulsion Laboratory

August 18, 1995

Contributors:

Marty Herman
Spacecraft Telecommunication Equipment Section
(818) 354-8541

Abhijit Biswas
P.I.: Vibrational Stress Metrology
(818) 354-2415

Elzbieta Kolawa and Beverly Tai
Advanced Materials and Fluid Processes Technology Group
(818) 393-2593

I.   Objective

- Test survivability of membranes after thermal cycling and vibration testing
- Characterize stress of membranes using vibrational analysis.

II.   Description of Membrane Structures

The membrane structures used for this study were fabricated at the University of Michigan. Two different sizes were used (see Figure 1). The shaded black area is the thermal oxide/SiN/oxide membrane with gold metallization and the white area is the supporting silicon wafer.
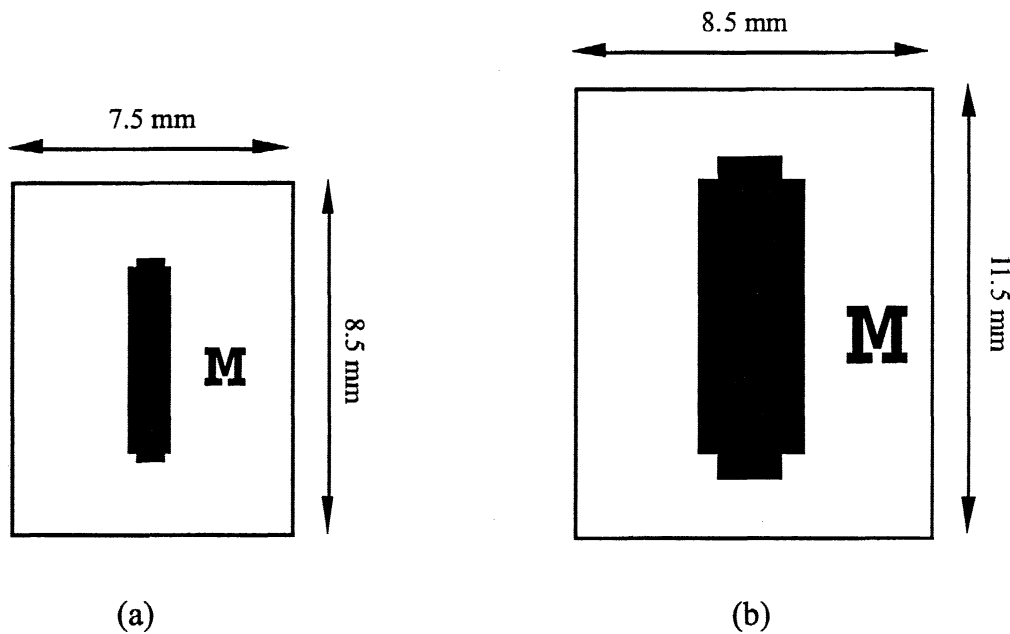

(a)   (b)

Figure 1:   Schematic of membrane structures: (a) Small and (b) Big.

The processing steps to grow the membranes were as follows (reference Tom Weller):

1. The first layer is a thermally grown silicon oxide that uses a standard CMOS process of dry-wet-dry growth. The typical furnace temperature is 1100°C. Dry oxide is grown with an oxygen flow rate of 3 L/min. Wet oxide flow rates are 1.7 L/min. oxygen and 2.5 L/min. nitrogen. The furnace temperature is about 800° C when the silicon wafers are inserted into the furnace, and it is ramped to 1100°C at about 5 deg./min.

2. The second layer is an LPCVD silicon nitride, grown at about 50-80 Å/min. The following parameters are used:
   LPCVD tilt zone temperatures: 810, 820, 830°C
   NH_3 160 sccm
   DCS (dichlorosilane)   40 sccm

3. The third and final layer is an LPCVD oxide, grown at about 50-80 Å/min. The following parameters are used:

LPCVD SiO_2 tilt zone temperatures: 910, 920, 930°C

N_2 (dilute)	290 sccm
N_2O	120 sccm
DCS	60 sccm

Typical layer thicknesses are 6500/3500/4500 Å (thermal oxide/nitride/oxide). These may vary ±500 Å. The membranes are typically about 1.5-2 mm wide, and the length ranges from 2.5 mm up to 10-12 mm. In some cases, 8mm x 8mm membranes have been used. The metallization is typically a gold layer which is 1-1.2 μm thick and covers more than 95% of the membrane surface. For the 8mm x 8mm membrane, however, the gold covers about 10% of the surface.

III. Thermal Cycling

Thermal cycling was performed in the Materials and Processes Lab at the Jet Propulsion Laboratory. The membrane structures were thermally cycled from $^-65$-$^+150$°C and inspected optically after 100 and 200 cycles. Please see "Results and Discussion" (Section V) for more detail.

IV. Vibration Testing

Sample Mounting
Samples were mounted on a steel block using two different adhesives: Adhesive one was a heavy viscosity, multipurpose, water soluble ultrasonic couplant and adhesive two was Eastman 910 glue. Adhesive one remained viscose during testing and was easily removed from the membrane structures after testing. However, due to adhesive one's viscosity, attenuation and sample displacement during testing was a concern. Therefore, adhesive two, which hardened seconds after application, was also used. Unfortunately, samples tested using adhesive two could not be removed from the steel block without breaking the membrane structures.

Test Parameters
Vibration testing was performed in the Environmental Test Lab at the Jet Propulsion Laboratory. The membrane structures were subjected to random vibration in each of their three principle axes, as shown in Figure 2. Figures 3-5 show the data plots for the control accelerometer of each axis. The random test profile is a modified version for what is specified in the reference for "Extended Exposure with Severe Radiation" for spaceborne computer modules. As modified, these vibration levels should provide a high level of confidence in the capability of the membrane structures to withstand any subsequent electronics higher assembly dynamics test exposure or flight environment even though not every potential resonance peak may be enveloped in these vibration test parameters.
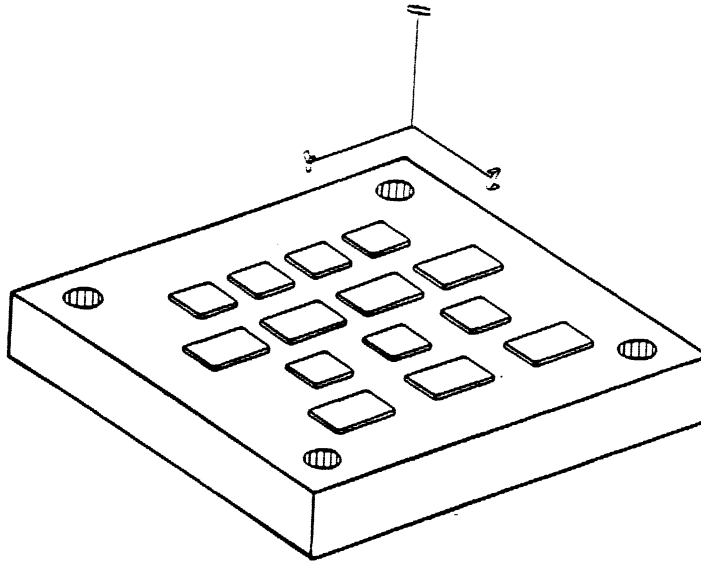
Figure 2: Axis definition and sample setup for vibration testing.

Vibration testing was performed as follows:

Random vibration qualification levels:

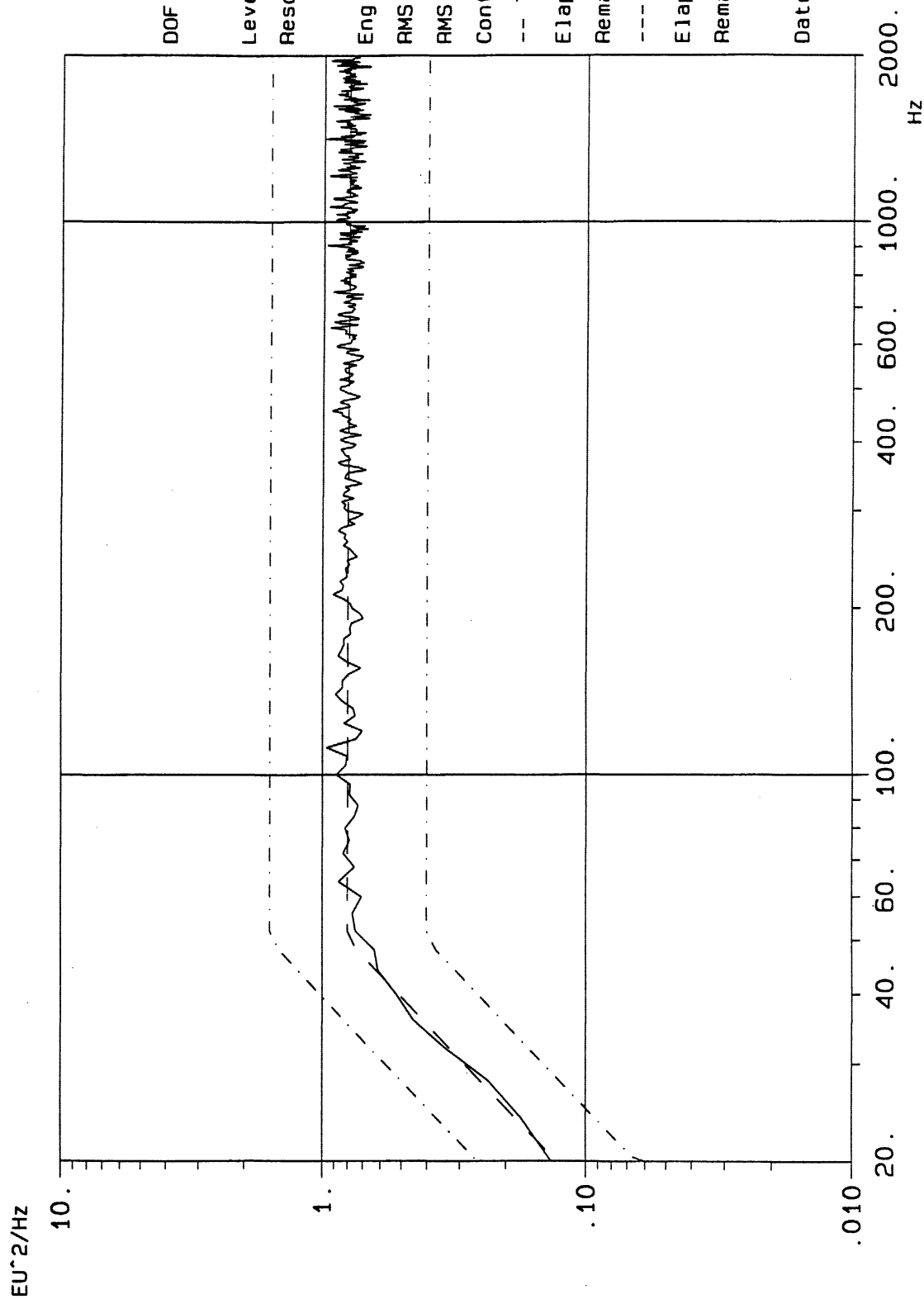| Frequency [Hz]	Level
20	0.129 g^2/Hz
20-50	$^+$6 dB/octave
50-2000	0.8 g^2/Hz

Overall: 39.6grms
Duration: 180 sec./axis

Test sequence:

Run #1:   X-axis random vibration, 0 dB for 180 seconds
Run #2:   Y-axis random vibration, 0 dB for 180 seconds
Run #3:   Z-axis random vibration, 0 dB for 180 seconds

Jet Propulsion Laboratory / Dynamics Testing

Random   Control

PDF

Run 1. X axis

EU^2/Hz

DOF   : 480

Level   :   0. dB

Resolution : 4. Hz

Eng. Unit : EU = g

RMS (act.) : 39.6977 g

RMS (ref.) : 39.6777 g

Contr. Mode: Closed loop

-- Time on act. level --

Elapsed   : 0:03:00

Remaining : 0:00:00

--- Time total ---

Elapsed   : 0:03:22

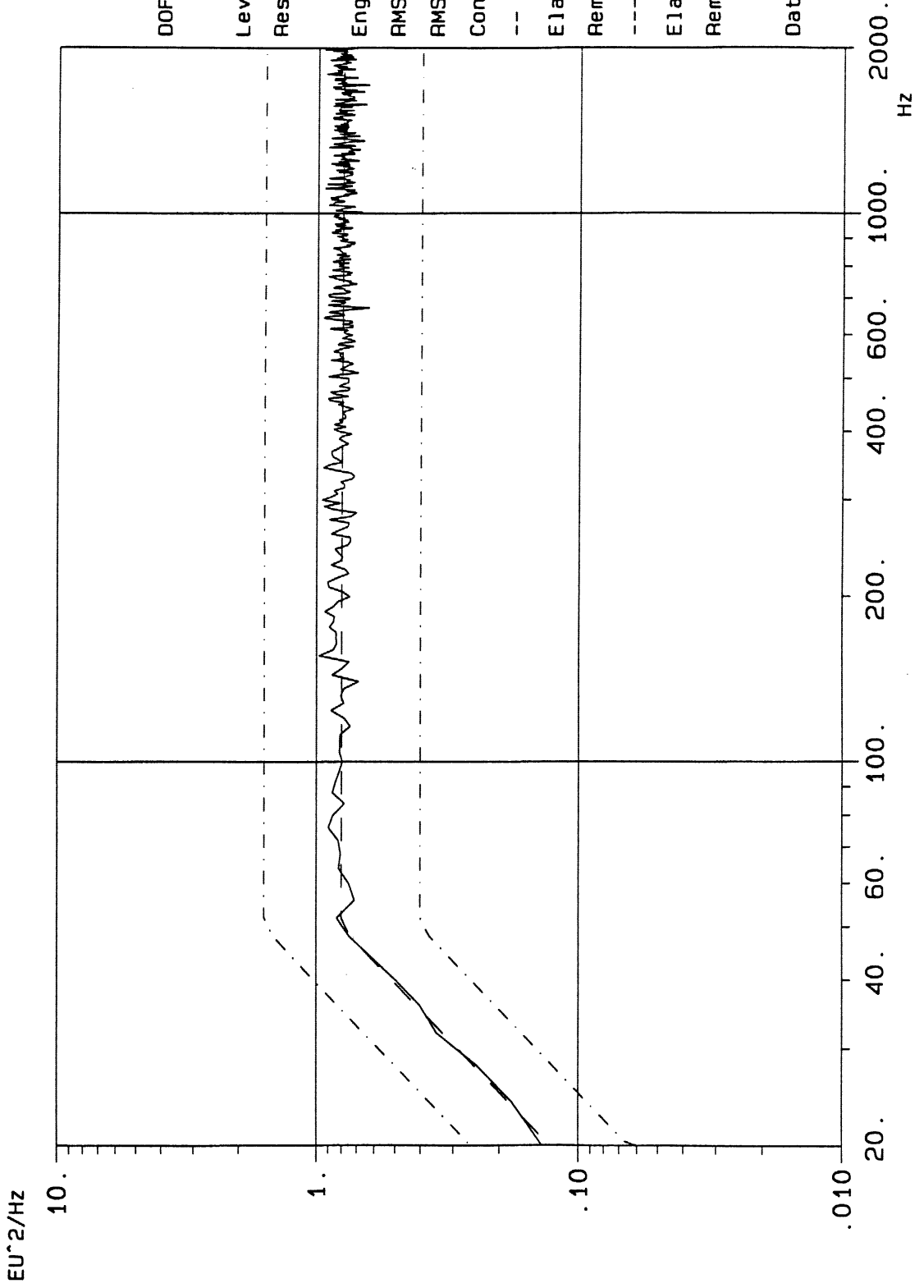Remaining : 0:00:00

Date : 5.31.1995

          9:10:49

Figure 3: X-axis

Jet Propulsion Laboratory / Dynamics Testing

Random   Control

PDF

Run 2, Y axis

EU^2/Hz

DOF   : 480

Level   :   0. dB

Resolution : 4. Hz

Eng. Unit : EU = g

RMS (act.) : 39.8449 g

RMS (ref.) : 39.6777 g

Contr. Mode: Closed loop

-- Time on act. level --

Elapsed   : 0:03:00

Remaining : 0:00:00

--- Time total ---

Elapsed   : 0:03:17

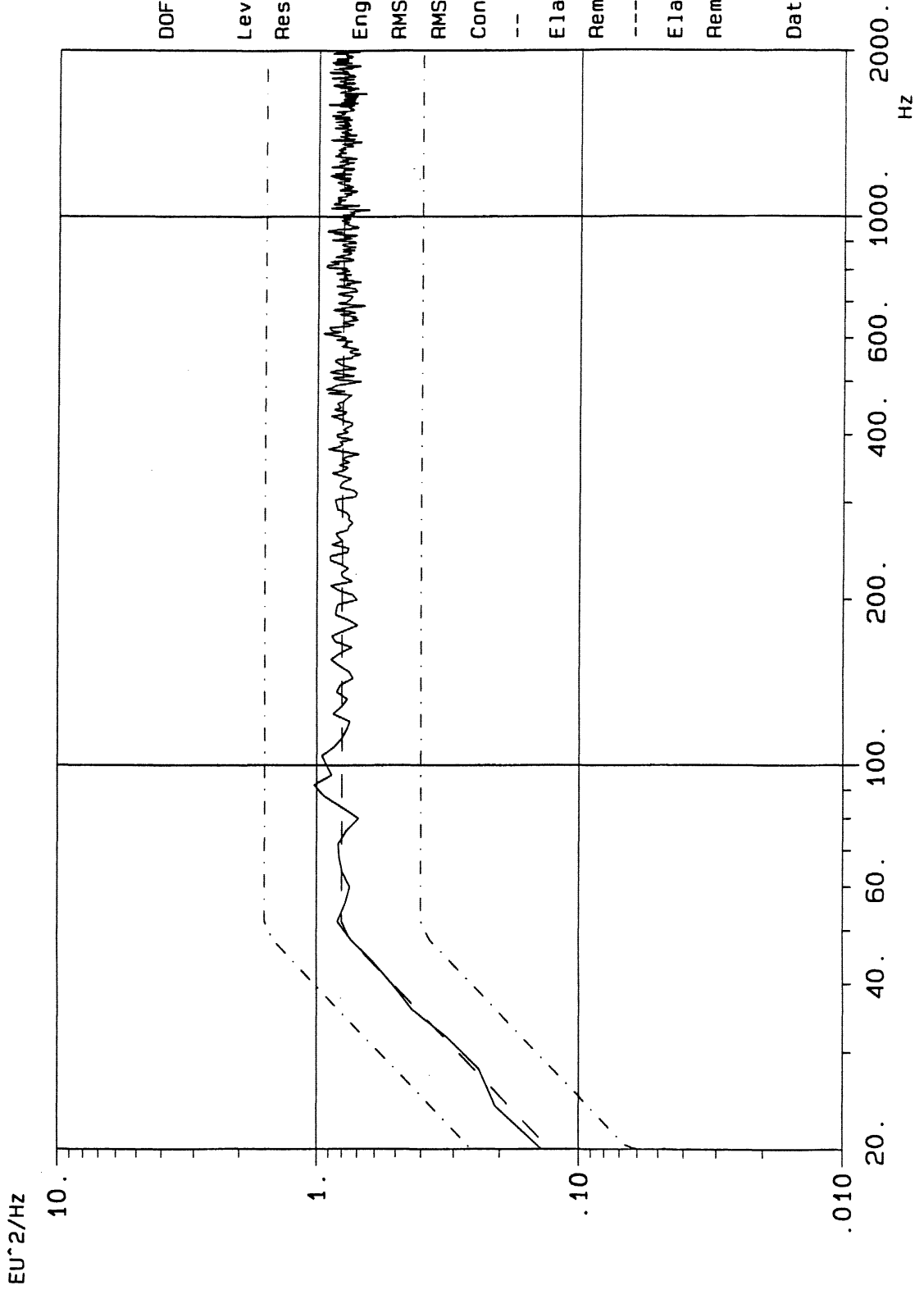Remaining : 0:00:00

Date : 5.31.1995
         9:28:25

Hz

Figure 4: Y-axis

Jet Propulsion Laboratory / Dynamics Testing

Random   Control

PDF

Run 3, Z axis

EU^2/Hz

10.

1.

.10

.010

20.   40.   60.   100.   200.   400. 600. 1000.   2000.

Hz

DOF   : 480

Level   :   0. dB

Resolution : 4. Hz

Eng. Unit : EU = g

RMS (act.) : 39.6352 g

RMS (ref.) : 39.6777 g

Contr. Mode: Closed loop

-- Time on act. level --

Elapsed   :   0:03:00

Remaining   :   0:00:00

--- Time total ---

Elapsed   :   0:03:15

Remaining   :   0:00:00

Date :   5.31.1995

   9:41:34

Figure 5: Z-axis

V.   Results and Discussion

Figure 6 shows the sequence of survivability tests performed and the number of samples tested. After vibration testing, membrane structures glued using adhesive two were inserted into the thermal cycling chamber while still on the steel block. However, these membranes ruptured after only one thermal cycle due to the lack of venting. All other membranes survived the thermal cycling and vibration testing without breaking, as determined by the careful examination of each membrane for signs of rupture using optical microscopy.
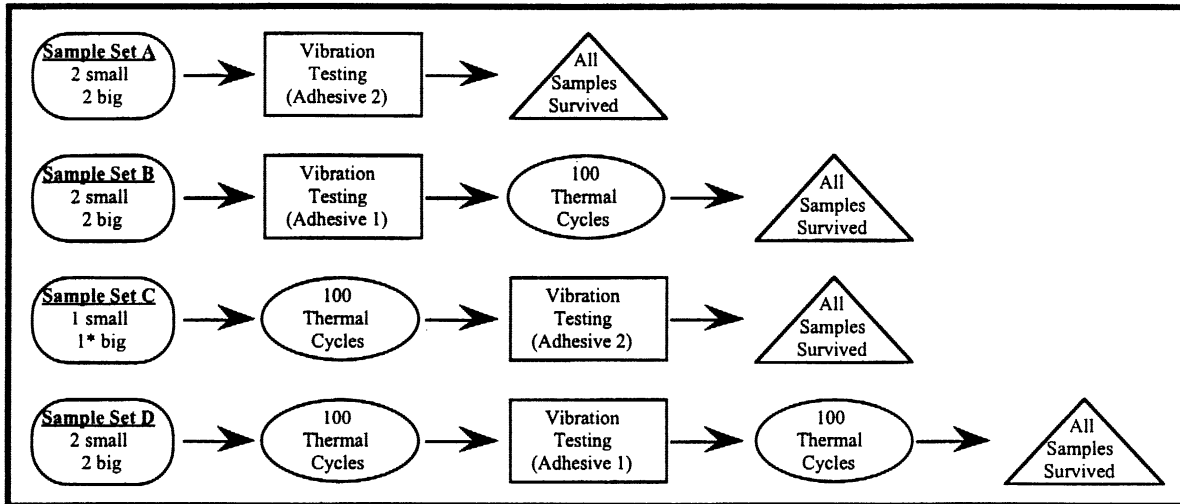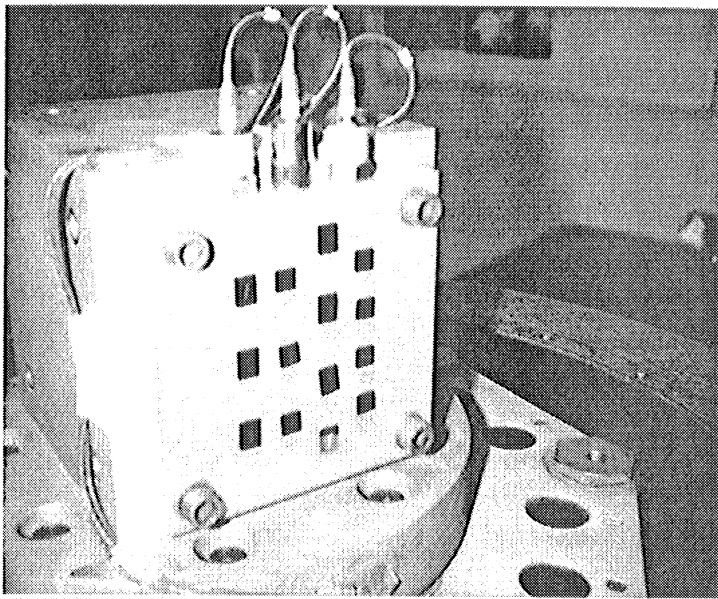

*Technician broke membrane after x-axis random vibration test.

Figure 6: Sequence of JPL survivability tests performed and number of samples tested.
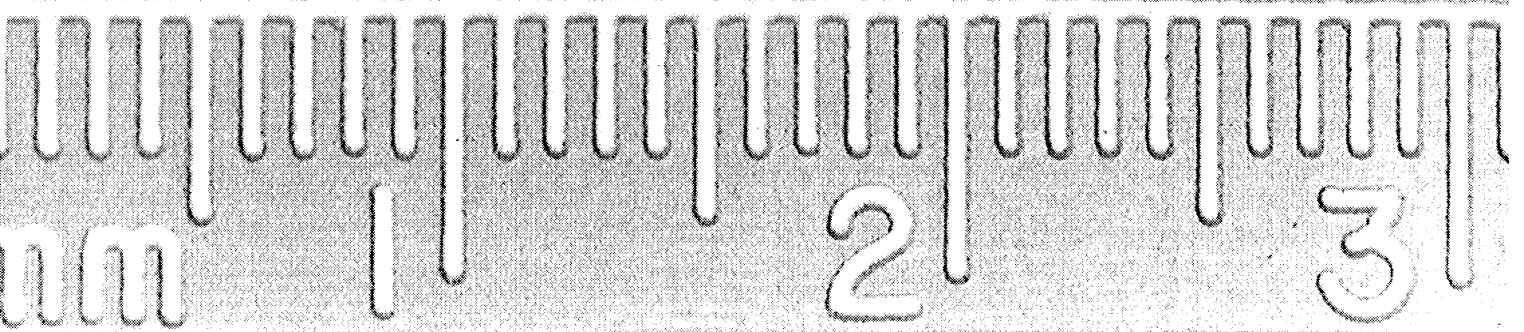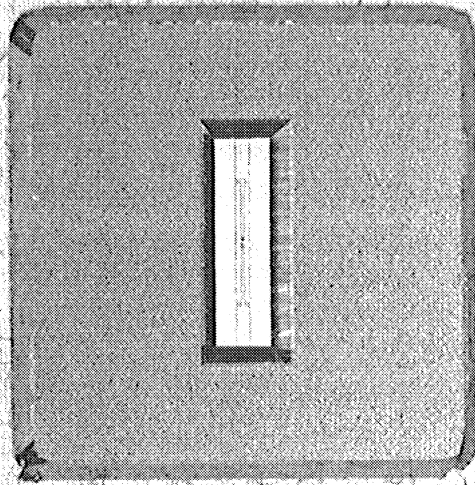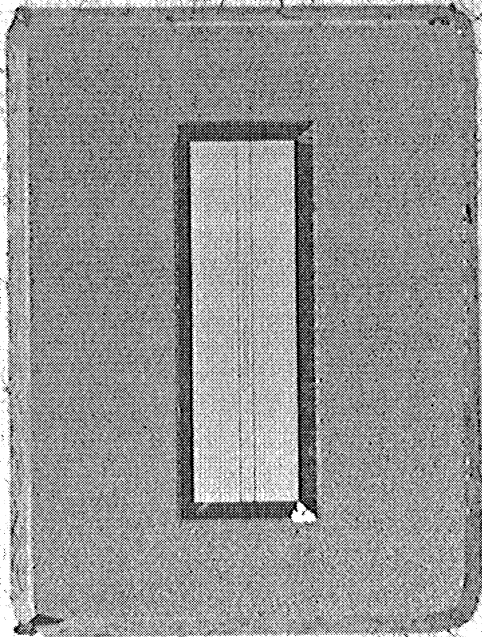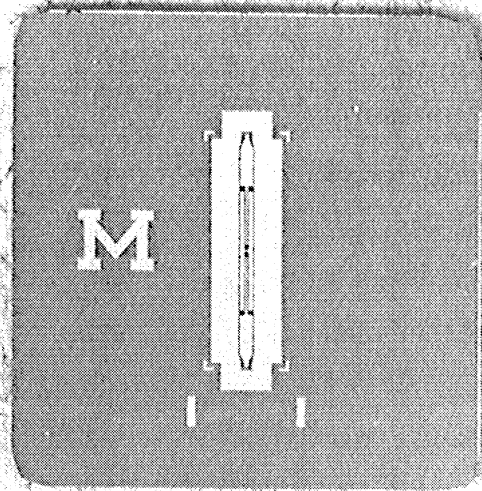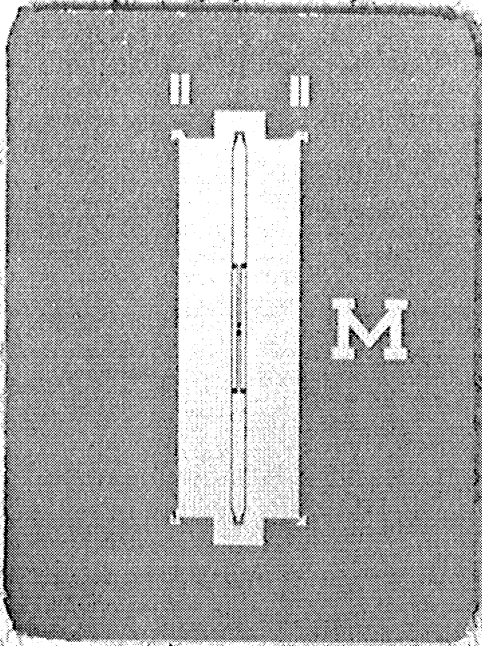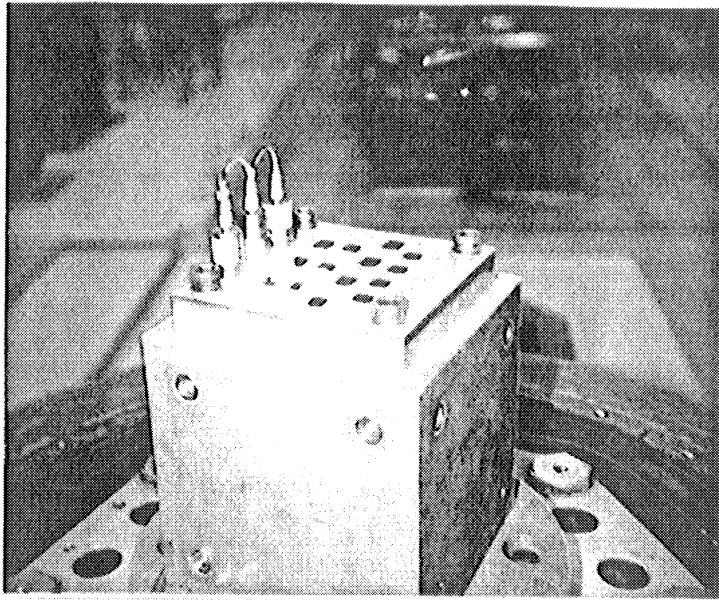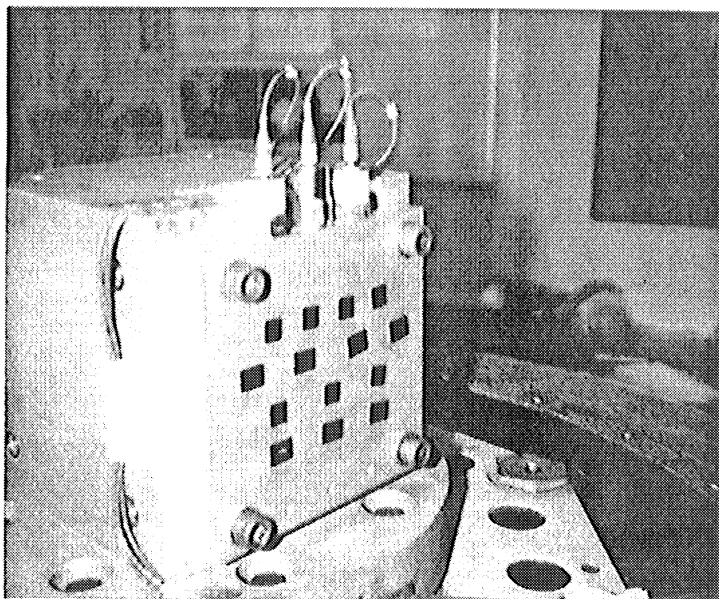
X-axis

Y-axis

Z-axis

Axis definition and sample setup for vibration testing.

Vibrational Stress Metrology

Introduction

A new technique is demonstrated for characterizing stress in membranes, since conventional approaches such as, x-ray rocking curve, and Raman spectroscopy do not work on amorphous membranes. Knowledge of the stress in supported membranes is critical for evaluating their eventual performance and reliability in applications, such as, transmission line technologies and x-ray lithography masks. Static and dynamic methods can be used for determining stress. In static techniques the stress is derived from membrane deflection in response to a known static pressure. The present report demonstrates a dynamic technique. Forced vibrations of the membrane are induced by external sinusoidal pressure fluctuations, where driving force frequency is varied, while recording membrane displacement with a laser vibrometer. At resonant frequencies the membrane exhibits displacement peaks. Thus a record of the frequency response of the driven membranes permits a determination of the resonant frequencies. The main advantage of our technique is the possibility of measuring displacement as a function of position on the membrane allowing an evaluation of modal response. The focused laser beam used for probing different regions allows the fine spatial resolution required for studying millimeter dimension membranes. Moreover the displacement measurements can be corroborated by surface velocity measurements using the same laser vibrometer, allowing a self-consistent approach to testing.

For a homogeneous rectangular membrane of density ρ (Kg/m^3) and under a uniform biaxial stress σ (N/m^2) the resonant frequencies f_{mn} are given by [1,2]:

$$f_{mn} = \frac{1}{2}\sqrt{\frac{\sigma}{\rho}}[(\frac{m^2}{Lx^2}) + (\frac{n^2}{Ly^2})]^{0.5}$$

where m and n are integers, 1,2,3....... Thus knowing f_{mn} and ρ allows a determination of σ. Lx and Ly are the membrane dimensions.

The membrane samples that are used in the present study are neither truly homogeneous, nor perfectly rectangular. Moreover, the damping forces which determine the spectral profiles of displacement versus frequency may vary over the membrane surface as a result of the metallization patterns used. A mathematical analysis based on finite element and finite difference techniques is called for, in order to model membrane response, thereby

facilitating interpretation of experimental results. However, in this preliminary study we treat the samples as homogeneous rectangular membranes with an assumed density.

f_{mn} obtained above is altered by atmospheric loading and the relation used to account for this fact is [3] :

$$f_{mn} = (f_{mn})_{air}[1 + 1.34(\frac{L\rho_{air}}{t\rho})]$$

where $(f_{mn})_{air}$ is the measured frequency from which the desired frequency can be obtained. ρ_{air} is air density, $L = \sqrt{(Lx.Ly)}$ and t is membrane thickness.

Experimental Setup

Dynamic testing of the membranes, at atmospheric pressure was conducted using the experimental setup shown in Figure 7a. Samples were mounted on a rigid support using double sided adhesive tape. The sample mount, laser vibrometer and speaker were supported on an air table in order to minimize noise interference from extraneous vibrations. Pressure fluctuations generated by the audio speaker (JBL Model 4370), excited membrane vibrations over a frequency range (10 - 46 KHz). The response of the membranes (displacement versus frequency) is interferometrically monitored by the laser vibrometer (Polytec PI Inc. Model OFV-302). A digital signal analyzer (HP Model 3562A) is used to perform frequency response scans on the membranes. A sinusoidal reference output fixed at 100 mV peak, is simultaneously applied to channel 1 of the digital signal analyzer (DSA) and the audio amplifier driving the speaker. Amplifier gain is adjusted to obtain desired output from the speaker. The analog, fringe counter output from the laser vibrometer controller, feeds channel 2 of the DSA. A frequency response scan is comprised of a linear sweep of frequency (resolution of 25-30 Hz) from the DSA reference. The ratio of power spectra (PS Channel 2 : PS Channel 1) is recorded during the scan. PS Channel 1 is flat since it originates from a fixed amplitude sinusoidal signal, thereby serving as a reliable reference. Relative variations in the PS Channel 2 are thus recorded, during the frequency response measurement. These variations correspond to laser vibrometer output, or, membrane displacement as a function of excitation frequency. Data transferred from the DSA to the computer contains both displacement and phase information of the membrane vibration, however, in the present report only displacement has been analyzed.

The output level of the speaker was chosen so that the membrane response could be discerned over the entire range of investigated frequencies. At the same time the laser vibrometer was used to probe regions of the substrate along the membrane boundary to ensure that it was <u>not</u> vibrating so that translational motion of the membrane did not interfere with the measurements. Laser vibrometer output was frequently recorded in the absence of excitation and the background noise was found to be 2-3 orders of magnitude lower than the driven response.

The measured frequency response of the membranes suffers from inherent output fluctuations of the speaker. Especially since a speaker is employed well beyond the audio range, its output cannot be assumed to be flat. A 1/4" microphone (Bruel & Kjaer, Model 4135) with a preamplifier (B & K Model 2618) and power supply (B & K Model 2801) was used to measure the speaker output. This was done after removing the mounted sample and positioning the microphone as close to the region occupied by the membrane as possible. The calibration of the microphone itself could not be checked, however, it is assumed to conform to its specifications of being flat within +/- 2 dB up to 100 KHz. Based on the microphone response the peak pressure applied to the membrane can be estimated to be in 1 - 5 Pa range.

Figure 7b shows a schematic top view of samples investigated. The blackened and hatched portions, respectively, represent the membrane and substrate. Three white spots on the membrane labeled 1, 2 and 3 mark locations where frequency response was monitored. Nominal membrane dimensions are also indicated in Fig. 7b. A set of membrane samples with smaller dimensions were also provided and await testing.

Results

Three samples with the dimensions indicated in Fig. 7b were tested. Table 1 summarizes the treatments of the samples.

Figures 8, 9 and 10 show the frequency response of each of the membranes following testing described above. Table 2 summarizes the frequency peaks observed at location 1 (see Fig 7b) for each of the samples. These frequency peaks are analyzed by studying the ratio $f_{mn}/f_{m'n'}$. Where m, n, m', n' denote the mode numbers of the resonance's. This

ratio is independent of the membrane density and atmospheric loading, depending only on membrane dimensions.

Table 1

Sample 1	As-deposited
Sample 2	Vibration testing ,100 thermal cycles (-65°C to 150°C)
Sample 3	100 thermal cycles (-65°C to 150°C), vibration testing, 100 thermal cycles (-65°C to 150°C)

Using this approach the mode numbers of the membrane vibrations were identified within an error of the indicated percentages. After correcting the observed frequencies for atmospheric loading membrane stresses can be obtained assuming that the homogeneous density of the membrane is 10083 Kg/m^3. The density value was obtained by weighting the relative thicknesses of $SiO_2/Si_3N_4/Au$.

Table 2

Sample 1		Sample 2		Sample 3	
$(f_{mn})_{air}$ KHz	m,n	$(f_{mn})_{air}$ KHz	m,n	$(f_{mn})_{air}$ KHz	m,n
22.173	1,1	23.841	1,1	18.188	1,1
25.145	1,2 (2%)	25.942	1,2 (6%)	19.855	1,2 (5%)
31.956	1,3 (5%)	32.608	1,3 (0%)	24.275	1,3 (3%)
37.753	1,4 (5%)	37.971	1,4 (2%)	28.985	1,4 (2%)
43.623	2,2 (2%)	44.492	1,5 (2%)	33.623	1,5 (3%)
				38.188	2,2 (5%)
				43.188	2,4 (3%)

Thus the following stresses are obtained

Sample 1 1.815×10^8 N/m^2

Sample 2 2.098×10^8 N/m^2

Sample 3 1.221×10^8 N/m^2

The stress values reported serve as a demonstration of the technique. Testing of a larger number of samples is required before any conclusions about stress dependence on treatment of the membranes can be derived.

The frequency response at the three probed locations are shown in Figures 8, 9 and 10. The relative displacement, as expected is highest at location 1. Qualitative differences in the spectral profiles, for instance between sample 1 and 2 (Fig. 8 and 9), where the same stress level is indicated deserve further study. The Polytec vibrometer used has not been independently calibrated but based on manufacturer's specifications the displacements observed in the spectra range from 10^{-7} - 10^{-8} m.

Conclusion

A new technique for measuring stress on supported membranes has been demonstrated. Further testing is required in order to characterize the stress level dependence on treatment and fabrication. A New Technology report on the technique described above is in preparation

References

1. L. F. Kinsler, A. R. Frey, A. B. Coppens, J. V. Sanders, "Fundamentals of Acoustics", Third Ed. J. Wiley & Sons, 1982, (Chapter 4)

2. P. M. Morse and K. Uno Ingard, "Theoretical Acoustics", McGraw-Hill Book Co., 1968, p.191.

3. M. Karnezos, "Effects of Stress on the stability of x-ray masks", J. Vac. Sci. Technol. B, 4, 226, 1986.
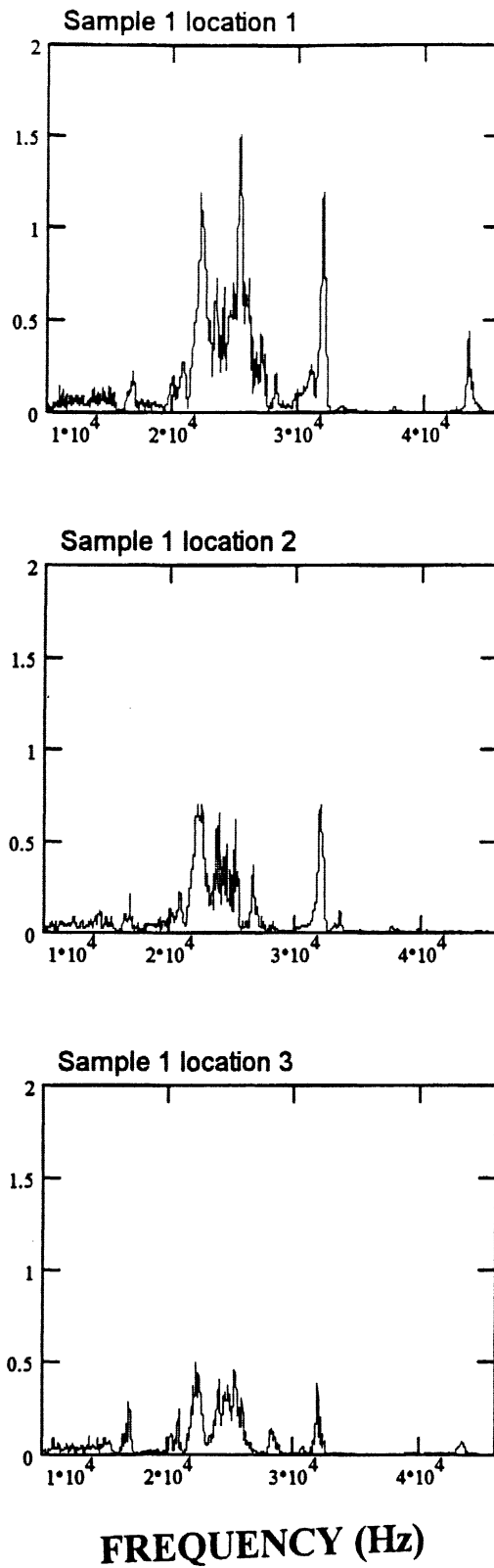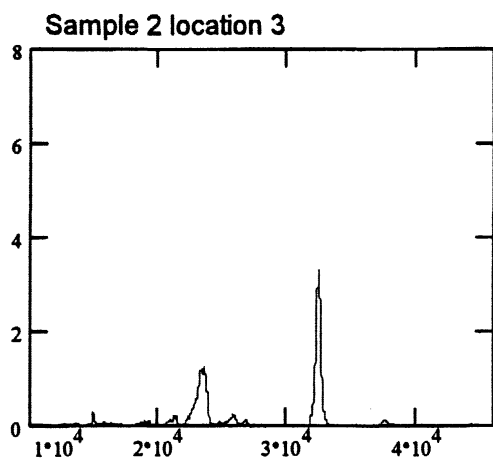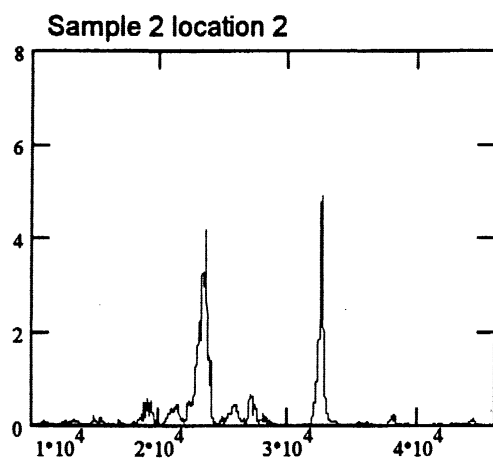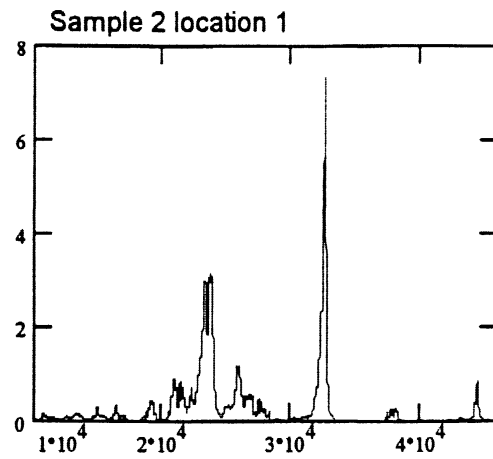
(a)

Speaker

Sample Mount

Lens   LASER VIBROMETER HEAD

microphone

AMP   COMPUTER   HP DSA 3562A   Ch2 Ch1 Ref   LASER VIBROMETER CONTROLLER

3   1   2

T 2.54 mm ⊥

|——— 6.85 ———|
mm

(b)

Figure 7   (a) A schematic view of the experimental arrangement used to measure stress in the membranes. The sample holder, laser vibrometer and speaker are all mounted on an air table;   (b) showing a top-view of the sample and the membrane dimensions.

Figure 8 Frequency response measured at different locations on Sample 1. The spectra have been corrected for variations in speaker output.

Figure 9 Frequency response measured at different locations on Sample 2. The spectra have been corrected for variations in speaker output.
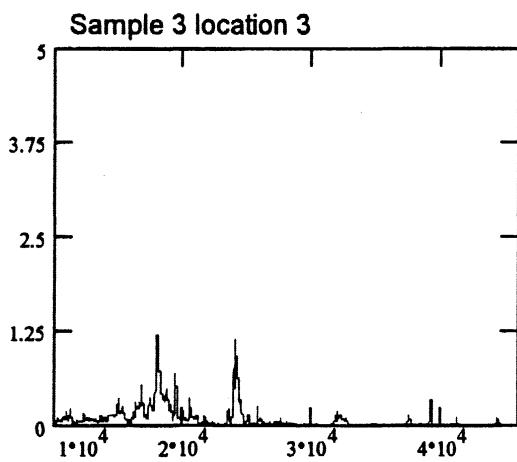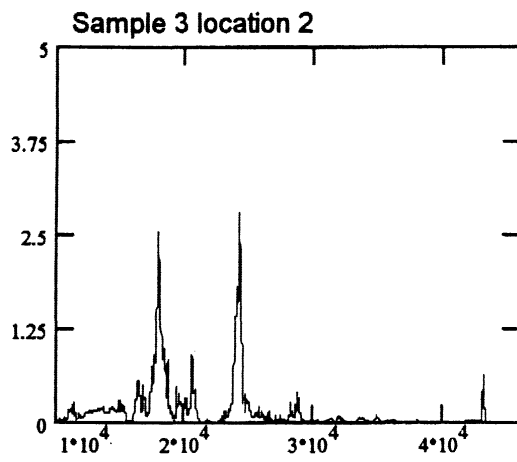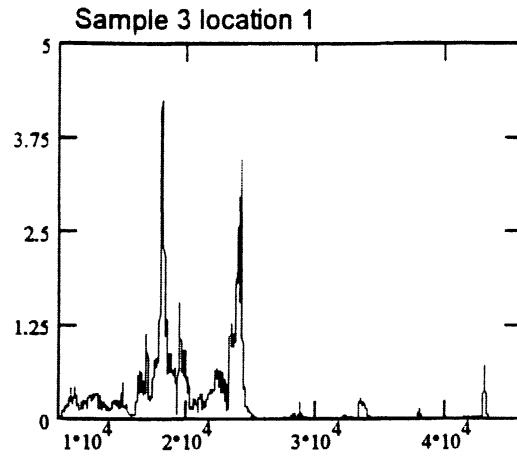
RELATIVE DISPLACEMENT

FREQUENCY (Hz)

Figure 10 Frequency response measured at different locations on Sample 3. The spectra have been corrected for variations in speaker output.